RESEARCH ARTICLE SUMMARY

PROTEIN INTERACTIONS

Autism mutations rewire protein interaction networks to drive neurodevelopmental pathology

Belinda Wang†, Rasika Vartak†, Kelsey M. Hennick†, Yefim Zaltsman†, Zun Zar Chi Naing† *et al.*

Full article and list of author affiliations: https://doi.org/10.1126/science.ady4523

INTRODUCTION: Autism spectrum disorder (ASD) is characterized by extreme genetic heterogeneity, with more than 250 high-confidence risk (hcASD) genes identified to date. Defined by rare, large-effect coding variants, these genes show functional and developmental convergence in transcriptomic analyses. However, these approaches have provided only limited mechanistic insight and have not identified specific therapeutic targets beyond the genetic variants themselves. Because proteins are the primary functional units of the cell, mapping the physical ASD interactome—and determining how ASD variants rewire it—is essential to move beyond gene lists and broad pathophysiologic themes toward a deeper causal understanding of neurodevelopmental pathology.

RATIONALE: To augment our molecular understanding of ASD, we used affinity purification–mass spectrometry (AP-MS) to map 100 hcASD proteins and 54 patient-derived missense variants, substantially expanding the known ASD protein interaction landscape. By integrating these datasets with AlphaFold structural modeling and functional studies in *Xenopus* and human forebrain organoids, we investigated whether genetically distinct risk factors converge onto shared biology and if convergent neurodevelopmental phenotypes arise through the selective rewiring of protein-protein interactions (PPIs) by disease-associated variants.

RESULTS: The resulting ASD-PPI network contains more than 1800 interactions, 87% of which were previously unreported. The network, which is enriched in neural progenitor cells (NPCs) of the excitatory lineage, exhibits a highly interconnected architecture, with risk proteins converging onto shared complexes, including DCAF7. Functional interrogation of selected interactions demonstrated that disruption of the previously uncharacterized DCAF7-DYRK1A-KIAA0232 complex impairs progenitor proliferation and reduces forebrain size in vivo. Furthermore, patient-derived missense mutations frequently induced convergent PPI rewiring. Distinct FOXP1 mutations, for example, weakened its physical interaction with FOXP4, leading to gain-of-function redistribution of FOXP4 to ectopic genomic targets. In human forebrain organoids, this biochemical rewiring drove premature differentiation of cortical neurons and altered neural activity. Genetic deletion of FOXP4 in a FOXP1-mutant background rescued these neurodevelopmental defects; although the exact mechanism requires further determination, this suggests that the rewired interaction underlies the mutant phenotype.

CONCLUSION: Together, these findings define a dual-layered model of molecular convergence in ASD: convergence through shared interaction networks in the wild-type state and convergence through recurrent functional consequences of interaction rewiring in the mutant state. More broadly, this work establishes a scalable framework for systematic interrogation of the autism proteome, enables prioritization of druggable protein interfaces, and provides a rational foundation for precision therapeutic strategies aimed at restoring neurodevelopmental trajectories. □

Corresponding authors: Nevan J. Krogan (nevan.krogan@ucsf.edu); A. Jeremy Willsey (jeremy@willseylab.com); Matthew W. State (matthew.state@ucsf.edu); Tomasz J. Nowakowski (tomasz.nowakowski@ucsf.edu); Kirsten Obernier (kirsten.obernier@ucsf.edu) †These authors contributed equally to this work. **Cite this article as B. Wang *et al.*, *Science* 393, eady4523 (2026). DOI: 10.1126/science.ady4523**

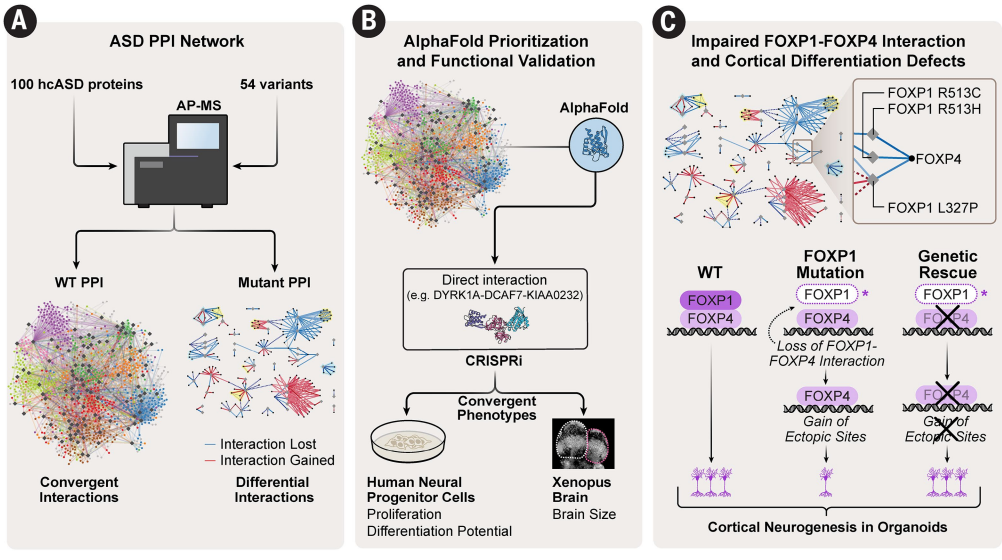

Mapping the ASD interactome reveals molecular convergence. (**A**) Protein interactome of 100 hcASD proteins and 54 patient mutations reveals a highly convergent network of protein complexes. (**B**) Convergent protein complexes were prioritized for functional validation in human neural progenitors and *Xenopus*. (**C**) Mutation-driven rewiring, such as FOXP1-FOXP4 interaction disruption, alters brain development, for example, deep-layer neurogenesis in cortical organoids in FOXP1 mutant organoids. R513C, Arg^{513}→Cys; R513H, Arg^{513}→His; L327P, Leu^{327}→Pro; CRISPRi, CRISPR interference; WT, wild type.

PROTEIN INTERACTIONS

Autism mutations rewire protein interaction networks to drive neurodevelopmental pathology

Belinda Wang[1]†, Rasika Vartak[2,3]†, Kelsey M. Hennick[1,4,5]†, Yefim Zaltsman[1]††‡, Zun Zar Chi Naing[2,3,6]†§, Benjamin J. Polacco[2,3], Ali Bashir[7], Manon Eckhardt[2,3], Mehdi Bouhaddou[2,3,6]¶, Jiewei Xu[2,3,6], Nawei Sun[1], Micaela C. Lasser[1], Yuan Zhou[2,3], Justin McKetney[2,3], Keelan Z. Guiley[7], Pawel Gniewek[7], Una Chan[8], Naufa Amirani[8], Owen Griffiths[1,4,5], Nishant Chadha[1,4,5], Reshmi Tognatta[2,3], Merve Cakir[2,3], Martin Gordon[2,3], Prachi Khare[2,3], Sam Drake[1]#, Vanessa Drury[1]**, David F. Burke[9], Silvano Gonzalez[1], Sahar Alkhairy[10], Reuben Thomas[3], Stephanie Lam[8], Montana Morris[1]††, Ethel Bader[1], Mélanie Dos Santos[11], Anastassia V. Komarova[11], Maxwell Bennett[2,3], Craig Ennis[2], Octavio Castillo[1,2], Yvonne Lim[2], Robert Martin[2], Meghan Seyler[1]‡‡, Tierney Baum[1]§§, Rebecca Krasnoff[1]¶¶, George Wang[1], Sagnik Middya[1,4,5], Sheng Wang[1], Presley Pham[1], Juan Arbelaez[1], Dexter Pratt[12,13], Sofia Bali[14], Shivali Chag[2], Julia A. Kaye[8,15], Nadir Mahmood[7]##, Lee Spraggon[2], Thomas Rolland[16], Shawn Hervey-Jumper[17], James S. Fraser[2,14], Thomas Bourgeron[16], Steven Finkbeiner[8,15,18,19,20], Caroline Demeret[11], Danielle L. Swaney[2,3,6,19], Sourav Bandyopadhyay[7], Trey Ideker[12,13], Pedro Beltrao[9,21], Helen Rankin Willsey[1,22], Ruth Hüttenhain[2,3,6]†††, Kirsten Obernier[2,3]*, Tomasz J. Nowakowski[1,2,4,5,17,23]*, Matthew W. State[1,2,24]*, A. Jeremy Willsey[1]*‡‡‡, Nevan J. Krogan[2,3,6,14]*

Systematic mapping of protein-protein interaction (PPI) networks and determining how causal mutations rewire them in autism spectrum disorder (ASD) provide a powerful framework for uncovering disease mechanisms and therapeutic opportunities. Using affinity purification–mass spectrometry, we systematically mapped PPIs for 100 high-confidence ASD genes, uncovering more than 1800 interactions. By assessing the impact of pathogenic missense mutations, leveraging AlphaFold, and validating key findings in human-derived model systems, we identified marked convergence onto shared protein complexes in the wild-type state and convergent PPI rewiring driven by independent mutations. For example, distinct patient-derived variants in FOXP1 disrupt its interactions with FOXP4, leading to changes in cortical neurogenesis and neural activity in brain organoids. Overall, these findings link genetic variation to protein networks and convergent neurodevelopmental dysfunction in ASD.

Autism spectrum disorder (ASD) is a highly heritable neurodevelopmental syndrome characterized by marked genetic heterogeneity and interindividual clinical variability (*1*–*3*). Over the past 15 years, whole-exome sequencing studies have identified more than 250 large-effect risk genes based on rare, often de novo, protein-damaging variants (*4*–*7*). These large-effect coding mutations are strongly enriched among the most severely impaired individuals with ASD and co-occurring neurodevelopmental disorders, including intellectual disability, epilepsy, minimal or absent speech, and severe motor delay.

Despite this progress, translating high-confidence ASD risk (hcASD) genes into a deeper understanding of pathophysiology—and ultimately into effective, targeted therapies for the most severe forms of the disorder—remains a major challenge (*8*). This difficulty stems from extensive pleiotropy, the dynamism of the developing human brain, and limited knowledge of the physical interactions of ASD risk proteins and how mutations alter the structure and function of these protein complexes (*9*, *10*). Two central unresolved questions are the degree to which diverse ASD proteins converge onto shared molecular complexes and how specific disease-causing mutations alter protein structure, interactions, function, and, ultimately, neurodevelopment.

One promising strategy is to examine bona fide ASD risk genes at the level of protein-protein interactions (PPIs) and whether disease-associated coding mutations selectively disrupt or rewire these interactions rather than simply abolishing gene function (*11*). If hcASD-associated mutations converge by rewiring shared protein complexes, then PPI networks should point to targetable causal mechanisms linking genetic variation to neurodevelopmental dysfunction. Testing this hypothesis requires systematic, large-scale, disease-relevant interaction maps that resolve both wild-type (WT) interactions and mutation-specific perturbations across a substantial fraction of the ASD proteome. However, such maps have been largely lacking.

Here, using affinity purification–mass spectrometry (AP-MS), we mapped PPIs for 100 hcASD genes and 54 patient-derived pathogenic variants (*4*). We generated these interaction maps in human embryonic kidney (HEK) 293 T cells to enable scalability and cross-disease comparability and then validated key findings across multiple experimental systems, including *Xenopus tropicalis*, human induced pluripotent stem cell (iPSC)–derived neural progenitors, and forebrain organoids. This approach revealed a dual-layered architecture of molecular convergence in ASD: stable convergence of risk proteins onto shared complexes in the WT state and convergent patterns of mutation-induced PPI rewiring.

We demonstrate that proteins interacting with these 100 ASD risk genes form a highly interconnected network that recapitulates ASD-relevant risk gene expression patterns in the developing human brain and is enriched for additional ASD risk genes, but not schizophrenia risk genes. Functional validation of key interactions confirms that these mutations perturb early neurogenesis and alter electrophysiological properties. Together, these results indicate that genetically heterogeneous ASD risk genes and distinct mutations converge onto complexes and rewire PPIs, providing a mechanistic framework linking genetic variation to protein structure and function and, ultimately, to convergent neurodevelopmental pathology.

PPI mapping reveals ASD networks

We evaluated structural and functional relationships among identified hcASD genes (*4*) (Fig. 1A) through the mapping of 100 Strep-tagged hcASD proteins individually expressed in HEK293T cells using AP-MS, generating an ASD PPI network (ASD-PPI) (Fig. 1B; fig. S1, A to C; and table S1). HEK293T cells provide the tractability, proteomic depth, and established benchmarks required for high-throughput PPI mapping. This approach has previously enabled the large-scale identification of bona fide, stable, and often stoichiometric physical interactions present across cell types for cancer, heart disease, neurodegeneration, and infectious diseases [for example, see (*12*–*19*)]. The resulting network connects 100 hcASD proteins with 1074 unique high-confidence interactors via 1881 total interactions. These include 87% previously unidentified interactions, with a median of 11 interactors per hcASD protein (Fig. 1, C and D). These interactions reveal strong interconnectivity among hcASD proteins and convergence onto shared interactors and complexes (see next sections). The ASD-PPI captures a broader interaction landscape than existing PPI databases (Fig. 1E) and overlaps substantially with previously published, smaller ASD-PPI networks generated in neuronal cultures or brain tissue (fig. S1D and table S1), thus supporting its biological relevance.

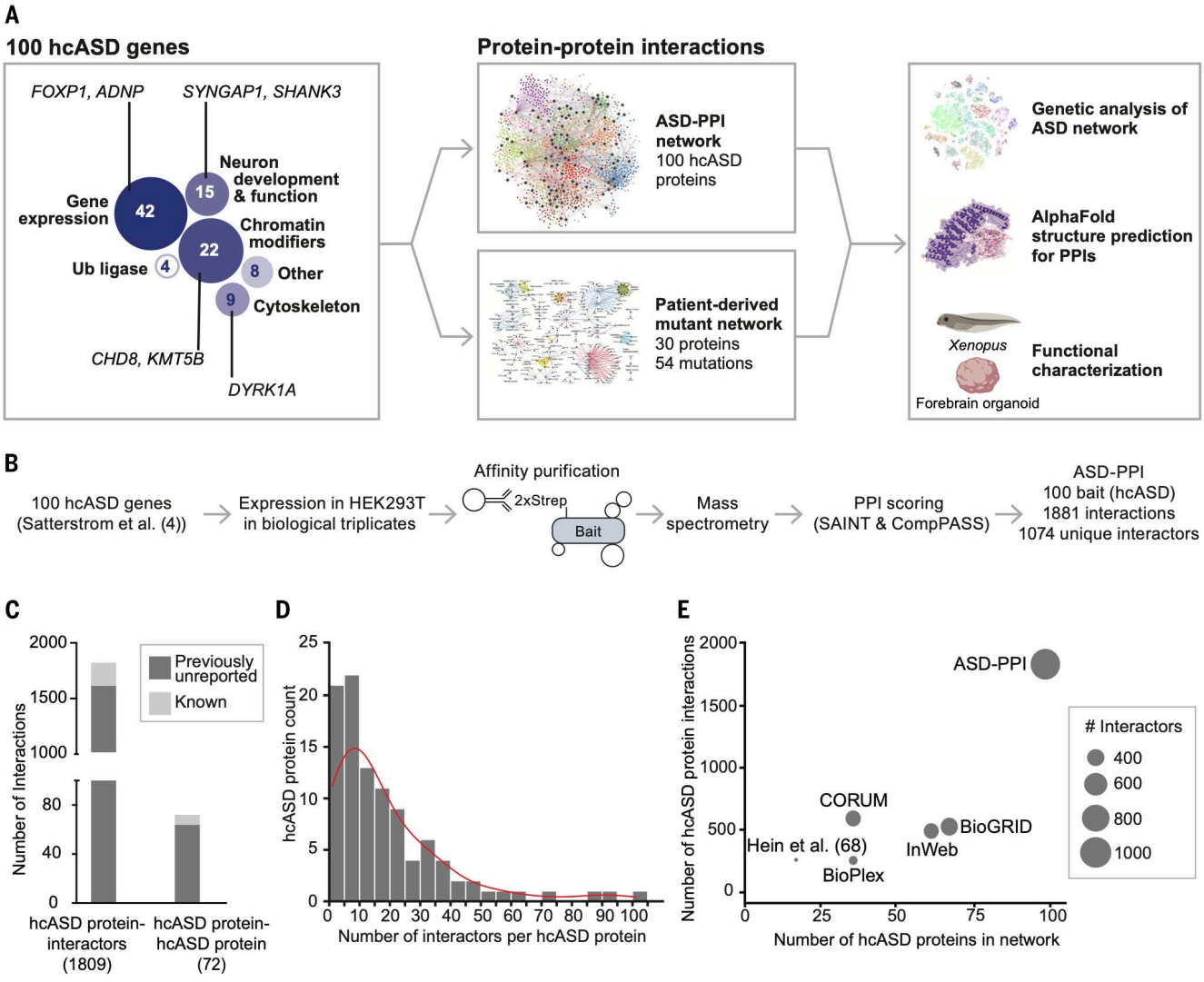

Fig. 1. hcASD protein interaction mapping reveals interactors. (**A**) Study overview showing prior functional annotations of 100 hcASD genes, highlighting the most significant two genes per category [FDR < 0.05; (*4*)], generation of WT (ASD-PPI) and patient-derived mutant (ASD_{mut}-PPI) interaction networks, and downstream studies. (**B**) Workflow to generate PPI data for 100 hcASD genes in HEK293T cells. (**C**) Bar graph showing distribution of interactions within the ASD-PPI. (**D**) The distribution of the number of interactors per hcASD protein (median = 11). The red line indicates the LOESS-smoothed curve of the distribution. (**E**) Comparison of the number of hcASD proteins profiled and the number of hcASD-associated interactions in ASD-PPI and existing large-scale PPI datasets (*54*,*67*,*68*,*89*,*90*). Point size reflects the number of unique interactors for each dataset.

[1]Department of Psychiatry and Behavioral Sciences, UCSF Weill Institute for Neurosciences, University of California, San Francisco, San Francisco, CA, USA. [2]Quantitative Biosciences Institute, University of California, San Francisco, San Francisco, CA, USA. [3]Gladstone Institute of Data Science and Biotechnology, J. David Gladstone Institutes, San Francisco, CA, USA. [4]Department of Anatomy, University of California, San Francisco, San Francisco, CA, USA. [5]Eli and Edythe Broad Center for Regeneration Medicine and Stem Cell Research, University of California, San Francisco, San Francisco, CA, USA. [6]Department of Cellular and Molecular Pharmacology, University of California, San Francisco, San Francisco, CA, USA. [7]Rezo Therapeutics, San Francisco, CA, USA. [8]Center for Systems and Therapeutics, Gladstone Institutes, University of California, San Francisco, San Francisco, CA, USA. [9]European Molecular Biology Laboratory, European Bioinformatics Institute (EMBL-EBI), Wellcome Genome Campus, Cambridge, UK. [10]Department of Computer Science and Engineering, University of California, San Diego, La Jolla, CA, USA. [11]Interactomics, RNA and Immunity, Institut Pasteur, Paris, France. [12]Department of Medicine, University of California, San Diego, La Jolla, CA, USA. [13]Institute for Genomic Medicine, University of California, San Diego, La Jolla, CA, USA. [14]Department of Bioengineering and Therapeutic Sciences, University of California, San Francisco, San Francisco, CA, USA. [15]Taube/Koret Center for Neurodegenerative Disease, Gladstone Institutes, University of California, San Francisco, San Francisco, CA, USA. [16]Human Genetics and Cognitive Functions, Institut Pasteur, UMR3571 CNRS, IUF, Université Paris Cité, Paris, France. [17]Department of Neurological Surgery, University of California, San Francisco, San Francisco, CA, USA. [18]Department of Neurology, University of California, San Francisco, CA, USA. [19]Department of Physiology, University of California, San Francisco, San Francisco, CA, USA. [20]Neuroscience Graduate Program and Biomedical Sciences Program, University of California, San Francisco, San Francisco, CA, USA. [21]Institute of Molecular Systems Biology, Department of Biology, ETH Zürich, Zurich, Switzerland. [22]Biohub, San Francisco, CA, USA. [23]Kavli Institute for Fundamental Neuroscience, University of California, San Francisco, San Francisco, CA, USA. [24]Langley Porter Psychiatric Institute, University of California, San Francisco, San Francisco, CA, USA. ***Corresponding author. Email: nevan.krogan@ucsf.edu (N.J.K.); jeremy@willseylab.com (A.J.W.); matthew.state@ucsf.edu (M.W.S.); tomasz.nowakowski@ucsf.edu (T.J.N.); kirsten.obernier@ucsf.edu (K.O.)** †These authors contributed equally to this work. ‡Present address: Maze Therapeutics, South San Francisco, CA, USA. §Present address: AstraZeneca, Boston, MA, USA. ¶Present address: Department of Microbiology, Immunology, and Molecular Genetics, University of California, Los Angeles, Los Angeles, CA, USA. #Present address: Altos Labs, South San Francisco, CA, USA. **Present address: Columbia University Mailman School of Public Health, New York, NY, USA. ††Present address: New York University Langone Medical Center, New York, NY, USA. ‡‡Present address: WAP Sustainability Consulting, Chattanooga, TN, USA. §§Present address: Department of Cell and Developmental Biology, Vanderbilt University, Nashville, TN, USA. ¶¶Present address: New York University School of Medicine, New York, NY, USA. ##Present address: Nkarta, Inc., South San Francisco, CA, USA. †††Present address: Department of Molecular and Cellular Physiology, Stanford, Stanford, CA, USA. ‡‡‡Present address: Calico Life Sciences LLC, South San Francisco, CA, USA.

ASD-PPI interactors are expressed in the human brain and enriched for ASD genetic risk

ASD-PPI interactors recapitulate core transcriptional and genetic features of ASD risk genes. In RNA sequencing (RNA-seq) data from developing (*20*) and adult human brain (*21*), the subset of interactors excluding hcASD genes (interactors$^{\text{no hcASD}}$, $n = 1043$) is highly expressed in brain tissue and closely tracks hcASD gene expression patterns across pre- and postnatal development (Fig. 2, A to C; fig. S2A; and table S2). This subset recapitulates core expression signatures of ASD-associated genes, including elevated expression in prenatal cortex (*22*) and adult cortex and cerebellum (fig. S2, B and C; and table S2) and shows intermediate evolutionary constraint greater than the HEK293T proteome but lower than hcASD genes (fig. S2D and table S2), suggesting that they may contribute to ASD through polygenic mechanisms. ASD-associated de novo damaging variants are enriched in both the full set of interactors (interactors, $n = 1074$) and interactors$^{\text{no hcASD}}$, but not in the rest of the HEK293T proteome (Fig. 2D and table S2), indicating that the interactors themselves are genetically associated with ASD. This enrichment magnitude is comparable to interactors from ASD networks generated in neuronal cultures (*23*) and from brain tissue (*24*, *25*) (fig. S2, E to G). ASD-PPI interactors also strongly overlap with ASD risk genes identified from recent large-scale sequencing studies (*5*–*7*), but not with genes implicated in schizophrenia (*26*), supporting a degree of specificity (Fig. 2E, fig. S2H, and table S2). To explore the potential of ASD-PPI for ASD gene discovery, we modeled networks of increasing size. As more hcASD genes are incorporated, enrichment of ASD-associated genetic variants progressively concentrates within interactors$^{\text{no hcASD}}$ (Fig. 2F) and captures a growing number of known and newly identified risk genes (hcASD+) (*6*), with no sign of saturation at 100 hcASD genes (Fig. 2G), suggesting that expanding the network could reveal additional risk genes. Together, these orthogonal analyses demonstrate that ASD-PPI captures ASD-relevant interactions.

To pinpoint ASD-relevant cell types, we examined ASD-PPI network expression in a prenatal human brain single-cell RNA-seq (scRNA-seq) atlas spanning cortical and subcortical cell types (*27*) (Fig. 2H). Previous studies have implicated postmitotic excitatory and inhibitory neurons (ENs and INs) (*4*, *6*). ASD-PPI shows strongest network expression in postmitotic ENs, with some enrichment in INs (Fig. 2I). However, expanding ASD-PPI by incorporating connections between interactors from the PPI meta database STRING (*28*) increases the statistical weight of the highly connected interactors in the network. This reframing from a risk gene–centric to interactome-centric view shifted the enrichment away from mature neurons and toward neural progenitor cells (NPCs) of excitatory neurons (NPC-ENs) and, to a lesser extent, of inhibitory neurons (NPC-INs) (Fig. 2I). This pattern was consistent across three independent prenatal brain atlases (fig. S2I and table S2) and recapitulated with a smaller network generated in neurons [iPSC-derived EN PPI network (iEN-PPI) (*23*); Fig. 2I]. These results indicate that ASD-relevant protein interactomes converge primarily on EN generation and early differentiation, a shift from prior reports that broadly implicated postmitotic neurons based on enrichment of hcASD genes alone (*4*, *6*).

ASD-PPI reveals molecular convergence

Organizing hcASD proteins and their interactors by connectivity and similarity in Gene Ontology annotations (*29*) (Fig. 3A and table S3) showed functional convergence consistent with previous results (*10*, *22*, *30*, *31*). The ASD-PPI network shows high connectivity: 31% of hcASD proteins interact with each other, whereas 35% of interactors bind multiple hcASD proteins (fig. S3A and table S3), suggesting functional overlap. Consistent with this, the network exhibits an increase in edge density and average node degree, measures associated with molecular convergence, while demonstrating low modularity (Fig. 3B and fig. S3B). This reflects a dense, interconnected landscape across hcASD proteins rather than segregation into isolated modules. These values are more extreme than those observed in previously published AP-MS networks organized around unified biological themes, such as tyrosine kinases [$n = 90$ (*32*)] or breast cancer genes [$n = 39$ (*12*)], indicating stronger molecular convergence in ASD-PPI (Fig. 3B and fig. S3B). Stratifying hcASD proteins by clinical phenotype [ASD-predominant (ASD_p) versus broad neurodevelopmental (ASD_{NDD}) (*4*)] shows no increase in interactor overlap, suggesting no functional distinction between these hcASD subgroups (fig. S3, B and C; and table S3).

Several hcASD proteins interact with protein complexes previously linked to ASD through both known and previously unknown interactions. These include the Sin3 complex [progenitor cell proliferation and differentiation (*33*, *34*)], the Mediator complex [transcription and neural stem cell identity (*35*, *36*)], and the PAF1 complex [progenitor proliferation and neuronal migration (*37*–*39*)], with subunits CTR9 and LEO1 near or just below the threshold for high-confidence ASD association (Fig. 3, C to E; and fig. S3, D and E). Although individual components of the PAF1 complex did not meet the statistical thresholds for hcASD genes (*4*, *6*), their high degree of connectivity to multiple hcASD proteins suggests a collective role in ASD pathobiology, consistent with recent clinical genetic evidence supporting PAF1 complex member LEO1 as an ASD risk gene (*40*). Additionally, 17 hcASD genes interact with the AP2-associated clathrin-mediated endocytosis complex (Fig. 3F), suggesting that these genes have diverse roles beyond gene regulation.

ASD-PPI is enriched for disease-relevant direct PPIs as predicted by AlphaFold

ASD-PPI includes both direct and indirect PPIs. To identify direct binding partners and their three-dimensional (3D) interaction interfaces, we repurposed AlphaFold-Multimer (AF) (*41*, *42*) to screen our ASD-PPI, which constrains the prediction of hcASD protein interactions across the human proteome to 1881 experimentally supported interactions (Fig. 4A and table S4). This included both hcASD-protein–interactor (hcASD-int; ASD-PPI) and interactor-interactor (int-int) pairs, the latter not directly assayed by our AP-MS. To identify a robust predictor of direct interactions, we evaluated several AF-derived metrics. The mean interface-predicted template modeling–score (mean ipTM) (*41*), which reflects the consistency and accuracy of predicted interaction interfaces, best distinguished hcASD-int pairs from negative controls (hcASD-random), with scores above 0.5 showing a 5- to 10-fold enrichment for likely direct contacts (Fig. 4B and fig. S4, A and B). This identified 113 high-confidence direct hcASD protein interactions [false discovery rate (FDR) 10 to 20%, 49 of 113 were previously unrecognized] (fig. S4C and table S4) and 466 indirect interactors connected to hcASD proteins via intermediate binding partners (int-int links; Fig. 4C and table S4). ASD-PPI showed nearly twice the rate of predicted direct interactions compared with iEN-PPI (*23*), suggesting that ASD-PPI is enriched for direct PPIs.

We validated a subset of predicted interactions using the NanoLuc (N2H) split luciferase binary interaction assay (*43*, *44*), confirming 12 of 37 tested pairs (~32%) as direct binders (fig. S4D), in range with N2H performance on known direct interactors and greater than the 10 to 15% typically observed for AP-MS data (*45*–*47*). Several pairs that were negative in N2H (for example, NUP155-SMPD4, SETD5-TBL1X, GNAI1-TNFAIP8, DYRK1A-KIAA0232, and DYRK1A-DCAF7) were confirmed by immunohistochemistry-based colocalization in NPCs, providing orthogonal support for their physical proximity (fig. S4E and also see fig. S5E). The previously unknown PPI and AF-predicted interaction between NUP155 and SMPD4 (Fig. 4G), a protein linked to microcephaly (*48*), highlights the approach's value for uncovering key interactions in neurodevelopmental conditions.

The interaction between hcASD protein DYRK1A and DCAF7 exemplifies a high-confidence AF interface prediction (Fig. 4, B and D to F). Although established (*49*), its 3D structure remains unsolved. The

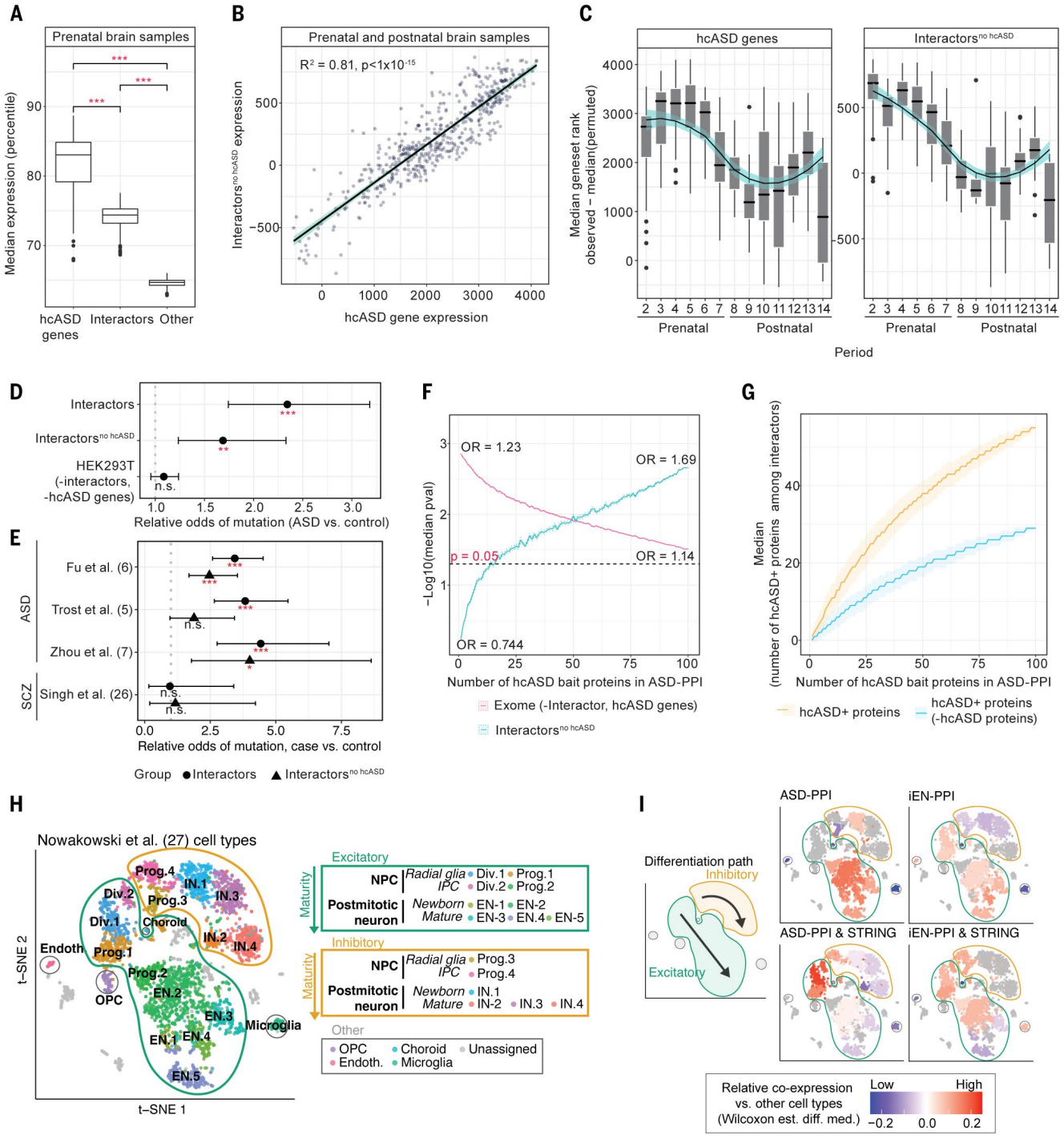

Fig. 2. ASD-PPI interactors are expressed in brain and enriched for ASD genetic risk. (**A**) Expression of hcASD genes, interactors$^{no\ hcASD}$, and other HEK293T proteins in prenatal brain (*20*). (**B** and **C**) Expression correlation of hcASD genes versus interactors$^{no\ hcASD}$ across 524 brain samples [Pearson's coefficient of determination (R^2) = 0.81, $P < 1 \times 10^{-15}$] (B) and developmental periods [(C) Spearman's correlation coefficient (ρ) = 0.946]. (**D** and **E**) Interactor enrichment for ASD de novo damaging mutations (D) and ASD or schizophrenia risk genes (*5*–*7*,*26*) (E). (**F** and **G**) Effect of bait number on interactor ASD risk enrichment (F) and hcASD+ recovery (G). Shading in (G) indicates ±1 SD from the median across 1000 permutations. OR, odds ratio. (**H**) Prenatal brain scRNA-seq t-distributed stochastic neighbor embedding (t-SNE) (*27*). Endoth., endothelial; Div., dividing; Prog., progenitor; OPC, oligodendrocyte precursor cell. (**I**) Relative coexpression of ASD-PPI and iEN-PPI networks across cell types with and without STRING. Color indicates edge coexpression relative to other cell types for nominally significant cell types ($P < 0.05$); gray indicates others. Data were analyzed by Student's *t* test (A), one-sided Fisher's exact test [(D), (F), and (G)], or Wilcoxon rank-sum test (I). Nominally significant is $P < 0.05$, and significant is Bonferroni-adjusted $P < 0.05$. For boxplots, the center line represents the median, box limits are the interquartile range (IQR), and whiskers are ±1.5 × IQR. For dot-whisker plots, OR is ±95% confidence interval (CI). n.s. is not significant, *0.01 < P < 0.05, **0.001 < P < 0.01, and ***P < 0.001.

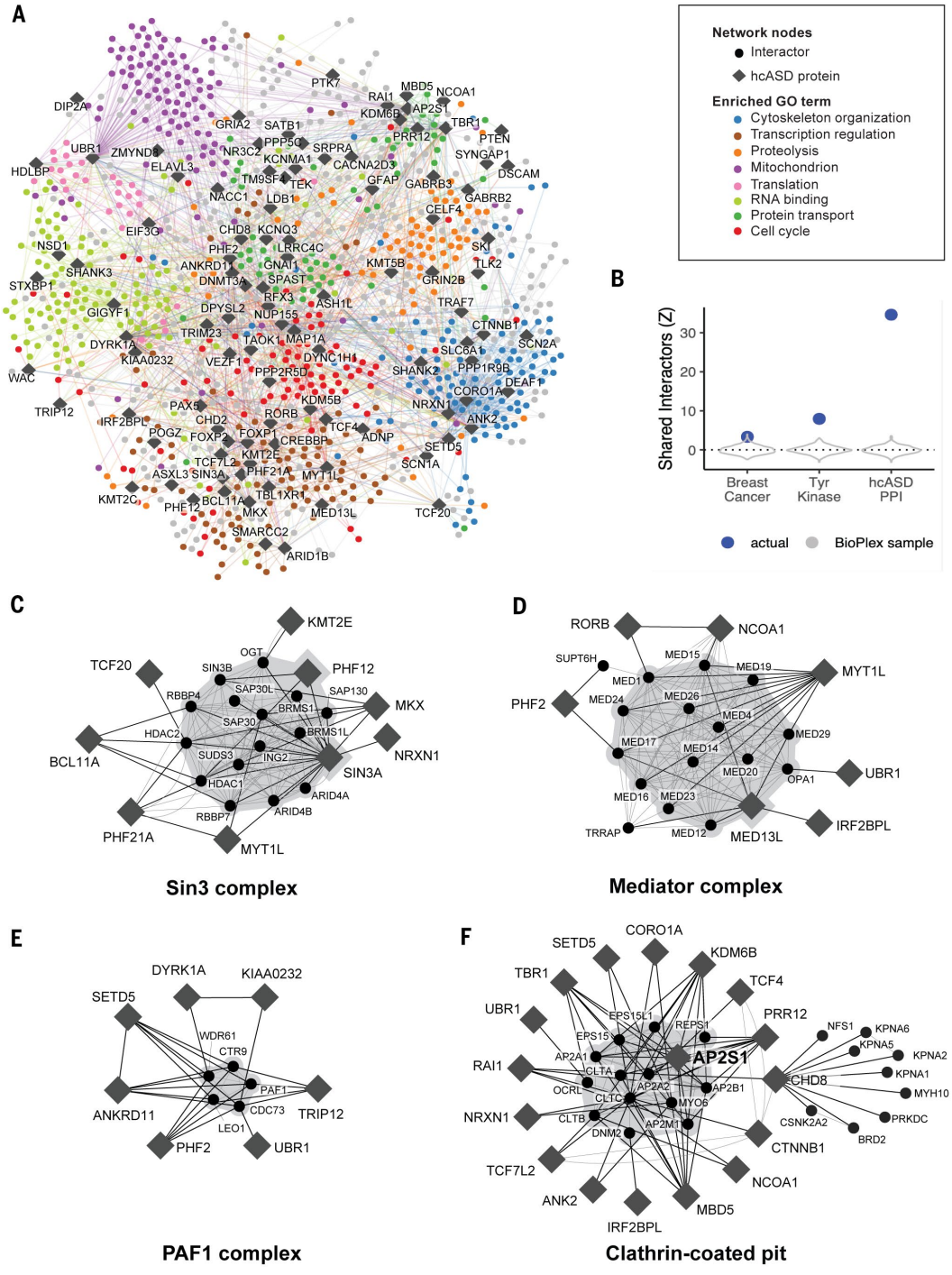

Fig. 3. ASD-PPI demonstrates molecular convergence among hcASD proteins. (**A**) ASD-PPI network map, with hcASD proteins and interactors positioned based on connectivity (AP-MS) and shared Gene Ontology (GO) terms. Interactor color reflects representative enriched GO categories that were selected to maximize coverage while minimizing redundancy. (**B**) Interactor overlap among bait pairs in ASD-PPI, breast cancer PPI (*12*), and kinome PPI (*32*), shown as the proportion of significant pairwise overlaps (hypergeometric $P < 0.05$). Proportions were converted to Z scores separately for each network by comparison with 1000 random degree-matched BioPlex networks (violins). (**C** to **F**) PPI networks showing hcASD protein interactions with the Sin3 (C), Mediator (D), PAF1 (E), and AP2-mediated clathrin-coated pit (F) complexes. Dark lines indicate AP-MS edges, thin gray lines indicate CORUM or STRING edges, and gray shading denotes CORUM complexes.

predicted interface matches the known DCAF7-binding region of DYRK1A (residues 80 to 100) (*50*) and shows high evolutionary conservation, consistent with selective pressure to preserve functionally important binding (Fig. 4, E and F). Deletion of this region (DYRK1A$^{\Delta 80\text{-}100}$) disrupts binding to DCAF7 but not to FAM54C, which binds the DYRK1A catalytic domain (residues 156 to 479) (*51*) (fig. S4F and table S4). These findings demonstrate the ability of AF to predict direct PPIs as well as the specific interfaces mediating these interactions. We further confirmed that AF-predicted interfaces can model the impact of patient mutations: Targeted mutagenesis of the GNAI1-RIC8A interface showed that binding affinity correlates with predicted pathogenicity (see next sections and fig. S8E).

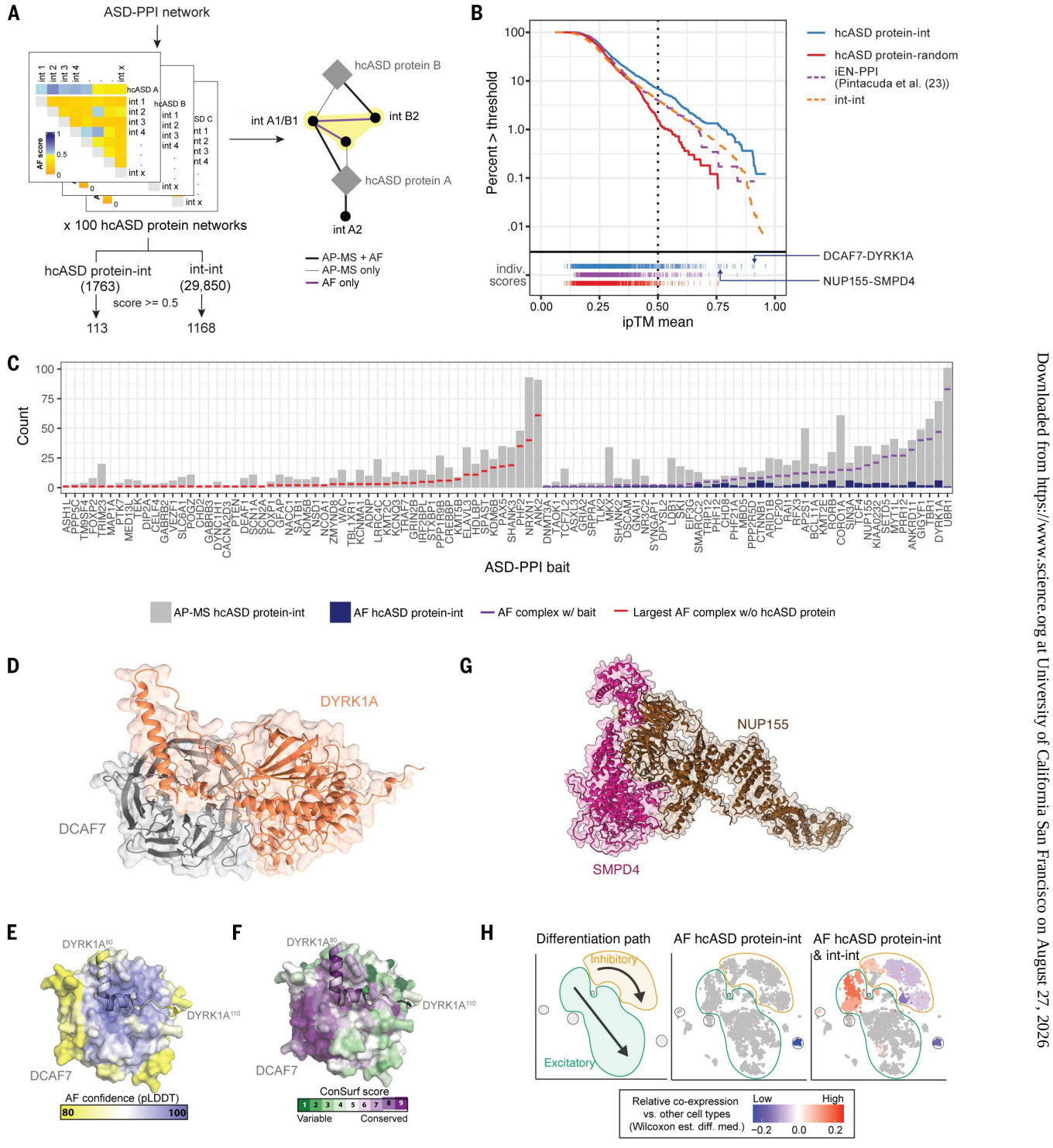

Fig. 4. AF predicts direct PPI interaction interfaces. (**A**) Workflow for AF interface predictions of hcASD-int ($n = 1763$) and int-int ($n = 29,850$) pairs. Example subnetwork shows AF-predicted edges linking two hcASD proteins via int-int interactions (purple). (**B**) Distribution of AF ipTM scores across PPI sets. The dotted line indicates the ipTM = 0.5 threshold, where hcASD protein-int pairs have ~5-fold enrichment over random controls. The comparison includes iEN-PPI (*23*) and hcASD-random (negative control). (**C**) Interactor counts per hcASD protein (gray), highlighting those predicted as direct by AF (blue). Purple lines denote interactors connected to hcASD proteins via AF-validated direct or mediated (int-int) paths. For hcASD proteins lacking direct AF edges, red lines indicate the largest AF-validated interactor complex. (**D** to **F**) AF-predicted DYRK1A-DCAF7 structure (D) colored by model confidence [predicted local distance difference test (pLDDT); (E)] or sequence conservation [ConSurf; (F)]. (**G**) AF-predicted NUP155-SMPD4 structure. (**H**) Relative coexpression of ASD-PPIs with or without AF int-int edges across brain cell types [(*27*); see Fig. 2H]. Color reflects relative network edge coexpression in each cell type compared with all others (Wilcoxon rank-sum test, estimated median difference). Nominally significant cell types ($P < 0.05$) are colored, and others are gray.

To determine whether the AF-supported direct interactome is enriched in specific cell types, we evaluated its expression across the three prenatal brain scRNA-seq cell atlases (*27*, *52*, *53*) as described above (see Fig. 2I and fig. S2I). The 113 AF-predicted direct hcASD-int pairs showed no cell-type enrichment; however, the inclusion of AF-predicted int-int connections led to an enrichment in NPCs, particularly NPC-ENs (Fig. 4H, fig. S4G, and table S4), consistent with our STRING-based findings (see previous sections; Fig. 2I and fig. S2I). This pattern was recapitulated with iEN-PPI (Fig. 2I and fig. S2I). Thus, the ASD interactome converges primarily on the generation and early differentiation of the excitatory lineage.

The DCAF7-DYRK1A-KIAA0232 complex regulates neurogenesis and differentiation

To further explore molecular convergence, we focused on seven "hub interactors" that bind eight or more hcASD proteins (Fig. 5A and fig. S3A). Only the DCAF7 interactome showed strong enrichment for additional ASD risk genes [hcASD+; (*6*)] in available interactomes (*54*), suggesting that hcASD proteins converge on DCAF7 (Fig. 5B and table S5).

DCAF7 is an adaptor protein that interacts with hcASD proteins such as DYRK1A, regulating its nuclear translocation and protein interactions (for example, with HAP1) (*55*), and AUTS2 and SKI to regulate neuronal lineage specification, highlighting its role in neurodevelopment (*56*). Comparing interactor overlap with DCAF7 and its binding hcASD partners revealed that hcASD proteins DYRK1A and previously uncharacterized KIAA0232 share substantial interactor overlap with DCAF7 (Fig. 5D and table S5), and AF predicted both to be direct DCAF7 interactors (table S4). Endogenous DYRK1A AP-MS in iPSC-derived iENs recovered DCAF7 and KIAA0232 and showed considerable overlap with HEK293T cell–derived interactors (fig. S5, A and B). Sequential AP-MS in HEK293T cells further confirmed that these three proteins physically interact as a complex, whose 126 shared interactors are enriched for hcASD+ (Fig. 5E and fig. S5, C and D). All three proteins localize to mitotic spindles in HEK cells and NPCs (fig. S5E), consistent with previous findings for DYRK1A in *Xenopus* and human NPCs (*57*, *58*). Furthermore, ASD-PPI interactors are enriched for proteins associated with mitotic spindle organization, such as centriolar satellites and centrosomes (fig. S5F and table S5).

We evaluated whether DCAF7, DYRK1A, and KIAA0232 share neurodevelopmental functions in vivo. Prior work showed that DYRK1A loss in *Xenopus* disrupts the cell cycle, increases apoptosis, and reduces telencephalon size (*58*). Using CRISPR-Cas9 mutagenesis in *Xenopus*, we found that knockout (deletion; KO) of *dcaf7* or *kiaa0232* phenocopies *dyrk1a* loss, reducing telencephalon size and linking this complex to an ASD-associated phenotype (Fig. 5F and table S5). To relate this to human clinical presentations, we analyzed cortical organoid scRNA-seq data from idiopathic ASD patients (*59*): The DCAF7-hcASD protein subnetwork was enriched among differentially expressed genes (DEGs) in normocephalic, but not macrocephalic, ASD (fig. S5G). This suggests that DCAF7 interactions contribute to ASD presentations without macrocephaly, consistent with the reduced forebrain growth observed in *Xenopus*.

To investigate cellular mechanisms, we used CRISPR-mediated knockdown (KD) in human iPSC-derived NPCs to reduce expression of DCAF7, DYRK1A, or KIAA0232. DCAF7 KD increased cell death during neuronal differentiation (fig. S5, H and I; and table S5), consistent with DCAF7's role in promoting cell viability (*60*). KD of either DCAF7 or KIAA0232 reduced the proportion of Ki67-positive NPCs, indicating impaired progenitor proliferation (fig. S5, J and K; and table S5). Global proteomics revealed coordinated changes after DCAF7 or KIAA0232 KD in NPCs (fig. S6A), enriched for hcASD+ and cell cycle, chromatin, and transcriptional regulators (fig. S6, B and C; and table S5). By contrast, DYRK1A KD modestly increased Ki67-positive NPCs (fig. S5, J and K), consistent with dose-dependent DYRK1A effects (*61*, *62*). Indeed, although *DYRK1A* mRNA was markedly reduced, global proteomics detected only a marginal decrease in DYRK1A protein amounts (fig. S6D), suggesting robust posttranscriptional buffering in NPCs. Despite this buffering, the expression of critical neurogenic transcription factors—PAX6, FOXG1, and SOX2—that are in part regulated by DYRK1A (*63*–*65*) was down-regulated upon KD of all three complex members (Fig. 5, G and H; and table S5). Collectively, these data indicate that disruption of the DCAF7-DYRK1A-KIAA0232 complex impairs neurogenesis across species.

hcASD gene missense mutations alter PPIs and result in convergent interaction changes

We next assessed how 54 patient-derived damaging de novo missense mutations predicted to be highly deleterious (*4*) across 30 hcASD proteins reconfigure PPIs (Fig. 6A and table S6). This mutant network (ASD_{mut}-PPI) identified 253 significantly altered interactions ($P < 0.05$), both gained or strengthened and lost or weakened (Fig. 6, B to D; table S6; and materials and methods). Lost interactions (136; 95 unique interactors) were enriched for hcASD proteins (fig. S7A and table S6), supporting a primary loss-of-function mechanism (*66*). Mapping these interactions in human NPCs confirmed strong overlap with our HEK293T data, with shared interactors significantly enriched for both mutation-sensitive and AF-predicted direct links (Fig. 6D, fig. S7B, and table S6), supporting network robustness across cellular contexts.

Given the convergence in ASD-PPI, we examined whether missense mutations in the same or across different hcASD genes cause shared protein interaction changes. In the 13 hcASD proteins with multiple variants, 45% of altered interactions were replicated across two or more mutants (for example, SLC6A1 and FOXP1 mutants; Fig. 6D and table S6). We additionally identified 15 interactors that showed consistent changes across two different hcASD mutants; for example, three FOXP1 mutants and one FOXP2 mutant lose interaction with FOXP4 (Fig. 6D; fig. S7, C and D; and table S6).

Integrating ASD_{mut}-PPI with other PPI networks (*23*, *54*, *67*–*70*) (see materials and methods, fig. S7E, and table S6) revealed that differential interactions consistently converge on the functional modules identified in the WT network (Fig. 3, C to F). For example, both MKX mutants [Arg^{93}→Gly (R93G), L89F] enhance interactions with the Sin3 transcriptional repression complex, whereas both MYT1L mutants (H522Q, C504R) reduce interactions with the Mediator complex, suggesting dysregulation of gene expression regulation. Similarly, both STXBP1 mutants (R551C, A251T) and both AP2S1 mutants (R10W, G64D) show stronger interactions with vesicle transport and clathrin complexes, respectively. Collectively, these findings indicate that patient-derived mutation-driven interaction changes converge on key biological processes that govern neurodevelopment. [Single-letter abbreviations for the amino acid residues are as follows: A, Ala; C, Cys; D, Asp; E, Glu; F, Phe; G, Gly; H, His; I, Ile; K, Lys; L, Leu; M, Met; N, Asn; P, Pro; Q, Gln; R, Arg; S, Ser; T, Thr; V, Val; W, Trp; and Y, Tyr.]

We next leveraged AF to prioritize direct interactions where an hcASD gene mutation is located at the predicted interaction interface (<10 Å; see materials and methods) (Fig. 7A). This identified 34 mutations across 22 hcASD genes at the interface of 216 interactions (table S7). Forty-six percent of interactions weakened in the mutant state are associated with a mutation at the interface, versus only 18% of strengthened interactions, suggesting that interface mutations are primarily disruptive (fig. S8A and table S7). For example, the PPP2R5D E198K mutation directly contacts the interaction interface (1.6 Å), leading to the loss of interaction with PPP4C (Fig. 7, B and C; and fig. S8B). By contrast, a mutation in GNAI1 I319T more distant to its interface with RIC8A (*71*) (6.1 Å) strengthens the PPI (Fig. 7, D and E; and fig. S8C). Targeted mutagenesis of this residue revealed that interaction affinity correlates with predicted pathogenicity: Whereas the benign variant I319V showed no change, three damaging variants altered RIC8A binding (fig. S8E). Finally, three FOXP1 missense variants evaluated in ASD_{mut}-PPI disrupt its interaction with FOXP4 (Fig. 7F) and are predicted to be highly pathogenic (fig. S8F and table S7). Despite residing

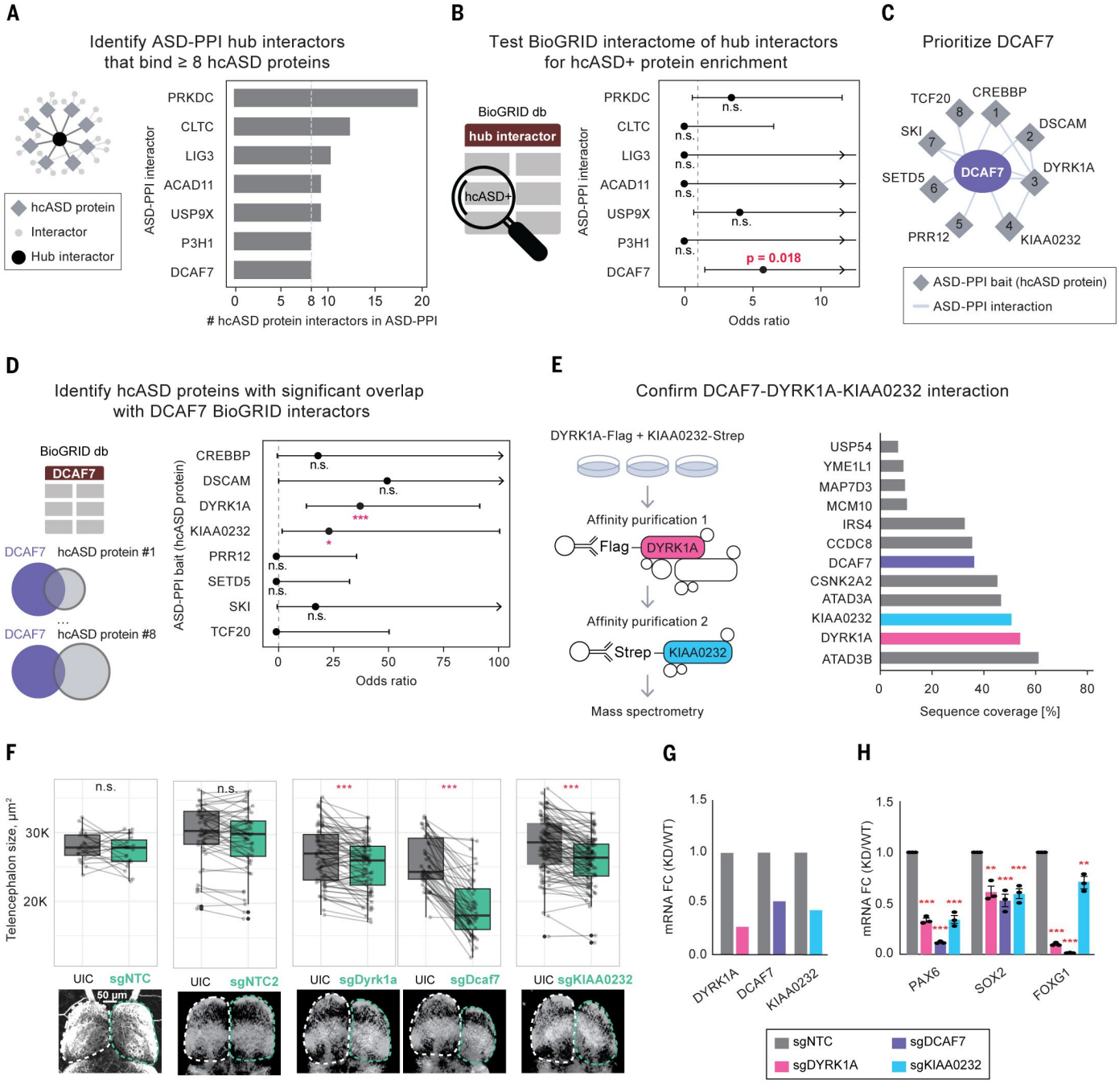

Fig. 5. DCAF7 forms a complex with multiple hcASD proteins. (**A**) ASD-PPI "hub" interactors binding ≥8 hcASD proteins. (**B**) Enrichment of hcASD+ in known interactomes of hub interactors from BioGRID (*54*). The dashed line indicates OR = 1 (no enrichment). (**C**) Hub interactor DCAF7 binds eight hcASD proteins in ASD-PPI. (**D**) Overlap between DCAF7 BioGRID interactors and ASD-PPI interactors of hcASD proteins bound by DCAF7. (**E**) MS sequence coverage from sequential immunoprecipitation of DYRK1A and KIAA0232. (**F**) *Xenopus* telencephalon size after unilateral single guide RNA (sgRNA) injection targeting Dcaf7, Dyrk1a, or Kiaa0232 versus nontargeting control (sgNTC). Scale bar is 50 μm. (**G**) CRISPR KD in NPCs of DYRK1A (pink), DCAF7 (purple), and KIAA0232 (blue) mRNA in respective cell lines. (**H**) Quantitative reverse transcription polymerase chain reaction (RT-PCR) in KD NPCs showing PAX6, SOX2, and FOXG1 expression versus NTC expression. Data were analyzed by Fisher's exact test (one sided, greater) [(B) and (D)], paired *t* test (F), or one-way analysis of variance (ANOVA) (H). *P* values are unadjusted (B) or corrected using the Bonferroni (D) or Dunnett (H) method. For dot-whisker plots in (B) to (D), dots represent OR, and whiskers represent 95% CI. For bar graphs, data are means ± SEM ($n = 3$ biological replicates). n.s. is not significant, $*0.01 < P < 0.05$, $**0.001 < P < 0.01$, and $***P < 0.001$.

at different structural locations—FOXP1 R513H at the DNA interface and FOXP1 L327P at the FOXP1-FOXP4 interface (Fig. 7G, fig. S8D, and movie S1)—all variants consistently weaken the FOXP1-FOXP4 association (Fig. 7, H and I), which led us to prioritize FOXP1 for additional functional investigation.

Collectively, our analysis of the WT and mutant networks revealed a dual-layered molecular convergence. First, the WT ASD-PPI identifies stable "molecular crossroads"—hub interactors such as DCAF7 that link disparate hcASD proteins into unified complexes. Second, the ASD_{mut}-PPI reveals a "functional convergence" of patient-derived variants;

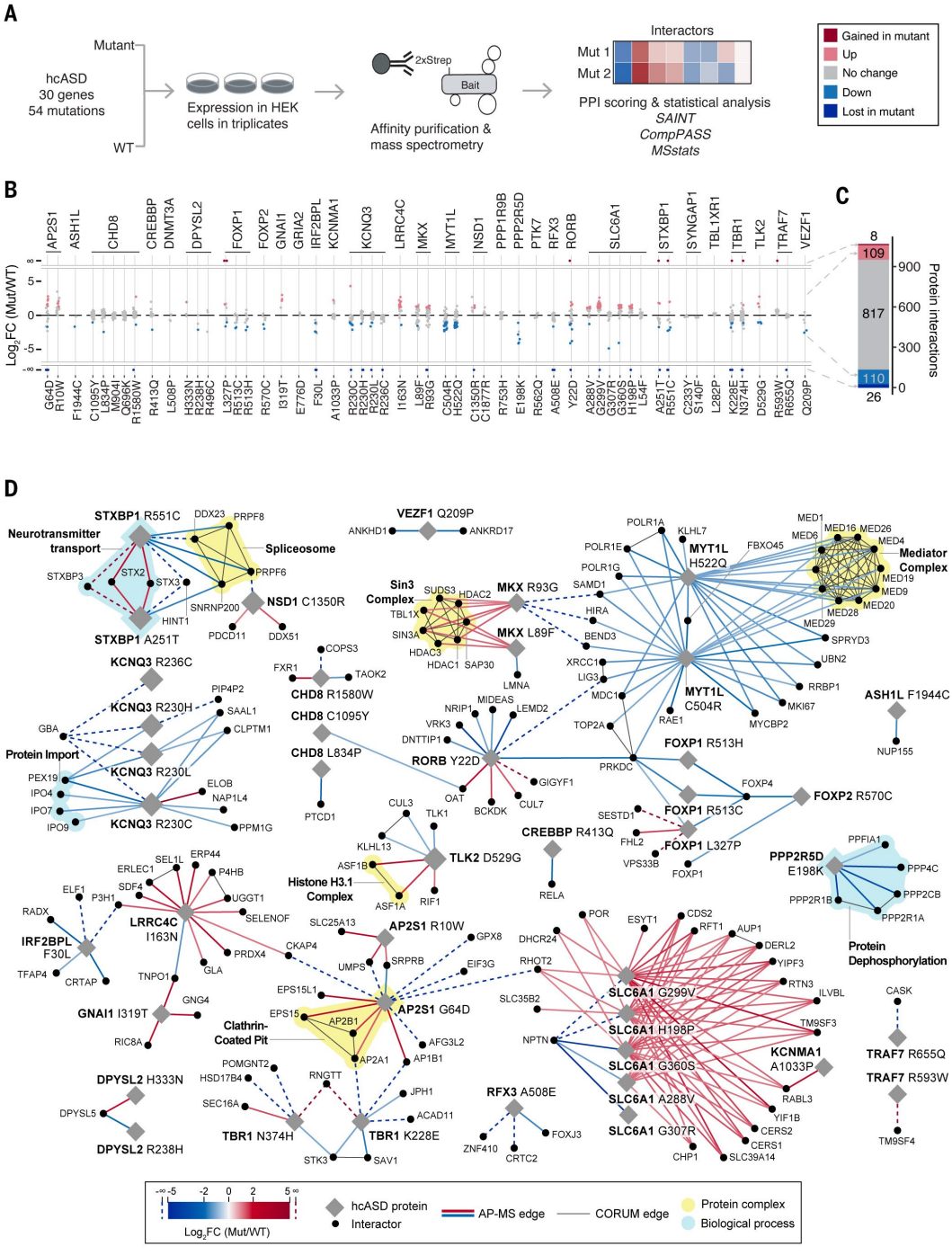

Fig. 6. Patient-derived hcASD gene missense mutations alter protein interactions. (**A**) Overview of the generation of the ASD patient-derived mutant network (ASD_{mut}-PPI). (**B**) Interaction changes between mutant and WT hcASD proteins, grouped by hcASD proteins with mutations labeled on the *x* axis. Significantly weakened (blue) or strengthened (red) hcASD protein interactions are highlighted, with mutant- or WT-specific interactions plotted at $\log_2$FC (fold change) = ∞ and −∞, respectively. (**C**) Quantification of differential protein interactions showing hcASD mutant–enriched interactions (red) and WT hcASD–enriched interactions (blue). (**D**) Network view of significant differential interactions in ASD_{mut}-PPI. Edge color reflects interaction specificity (blue, stronger in WT; red, stronger in mutant), and dashed edges indicate interactions specific to mutant or WT. CORUM protein complexes (yellow) and GO biological processes (blue) highlight functional modules disrupted within and across hcASD proteins. In (B) to (D), data were analyzed by pooled *t* test on intensity values, with FDR estimated using Storey's *q* method; interactors with $|\log_2FC(Mut/WT)| \geq 1$, FDR < 0.1, and $P < 0.05$ were considered significantly differential.

disparate mutations in the same genes, for example, *MKX*, *STXBP1*, and *AP2S1*, or different genes, for example, *FOXP1* and *FOXP2*, drive similar directional changes in interaction strength within their respective functional modules. This suggests that although ASD risk is genetically heterogeneous, the molecular consequences of these mutations collapse onto a limited set of vulnerable protein systems.

hcASD gene mutations alter cortical neuron differentiation

FOXP1 encodes a forkhead box domain–containing transcription factor expressed in early brain development (*72*–*75*). To identify neurodevelopmental processes disrupted by ASD patient variants, we generated isogenic iPSC lines with a $FOXP1^{R513H}$ allele, selected for its predicted high pathogenicity (Fig. 8, A and B; and fig. S8F). We confirmed the

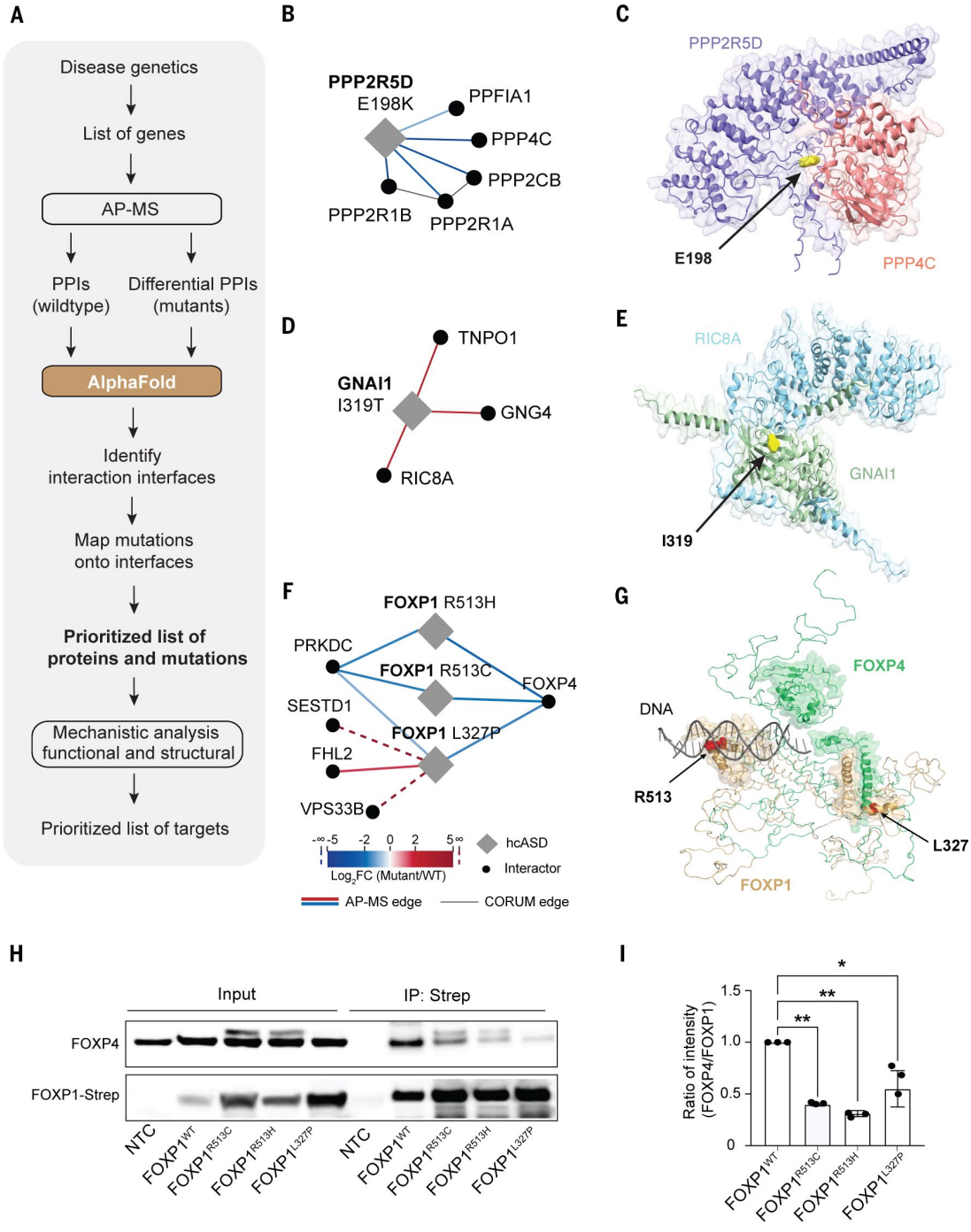

Fig. 7. AF maps hcASD gene mutations to protein structures and interaction interfaces. (**A**) Workflow to prioritize protein interactions affected by hcASD gene mutations using AP-MS and AF structure predictions. (**B**, **D**, and **F**) Differential ASD_{mut}-PPI networks for $PPP2R5D^{E198K}$ (B), $GNAI1^{I319T}$ (D), and $FOXP1^{R513H}$, $FOXP1^{R513C}$, and $FOXP1^{L327P}$ (F). Edge colors and significant differential interactions are as in Fig. 6D. (**C**, **E**, and **G**) AF-predicted interactions for PPP2R5D-PPP4C with E198 at the interaction interface (C), GNAI1-RIC8A with I319 at the interaction interface (E), and model of the FOXP1-FOXP4 (yellow-green) complex visualizing the relative flexibility of structured DNA binding and coiled-coil domains (shown in surface rendering) mediated by interspacing intrinsically disordered regions (coil). Highlighted in red are FOXP1 residues R513 at the FOXP1 DNA-binding interface and L327 at the FOXP1-FOXP4 dimerization interface (G). (**H**) IP–Western blot of nontransfected control (NTC) or Strep-tagged $FOXP1^{WT}$, $FOXP1^{R513C}$, $FOXP1^{R513H}$, or $FOXP1^{L327P}$ in HEK293T cells. (**I**) Quantification of data from (H). Data are shown as means ± SEM ($n = 3$ biological replicates). Data were analyzed by one-way ANOVA with Dunnett's correction; adjusted P (P_{adj}) = 0.0011 ($FOXP1^{R513C}$), $P_{adj} = 0.0018$ ($FOXP1^{R513H}$), and $P_{adj} = 0.0141$ ($FOXP1^{L327P}$).

loss of FOXP1-FOXP4 interaction in $FOXP1^{R513H/WT}$ iPSC-derived NPCs (fig. S9A) and assessed cell-type composition in organoids using immunostaining at time points that correspond to early (day 39) and late cortical neurogenesis (day 101) (*76*). During early neurogenesis, we found a reduction in $PAX6^+$ progenitor cells and an increase in the abundance of both $BCL11B^+$ layer V neurons and $TBR1^+$ layer VI/subplate neurons in $FOXP1^{R513H/WT}$ compared with $FOXP1^{WT/WT}$ (Fig. 8B). At day 101, we found no difference in the abundance of $PAX6^+$ cells, but a reduction in $BCL11B^+$ cells in $FOXP1^{R513H/WT}$ organoids (Fig. 8B). The abundance of $TBR1^+$ cells was lower in $FOXP1^{R513H/WT}$ than in $FOXP1^{WT/WT}$,

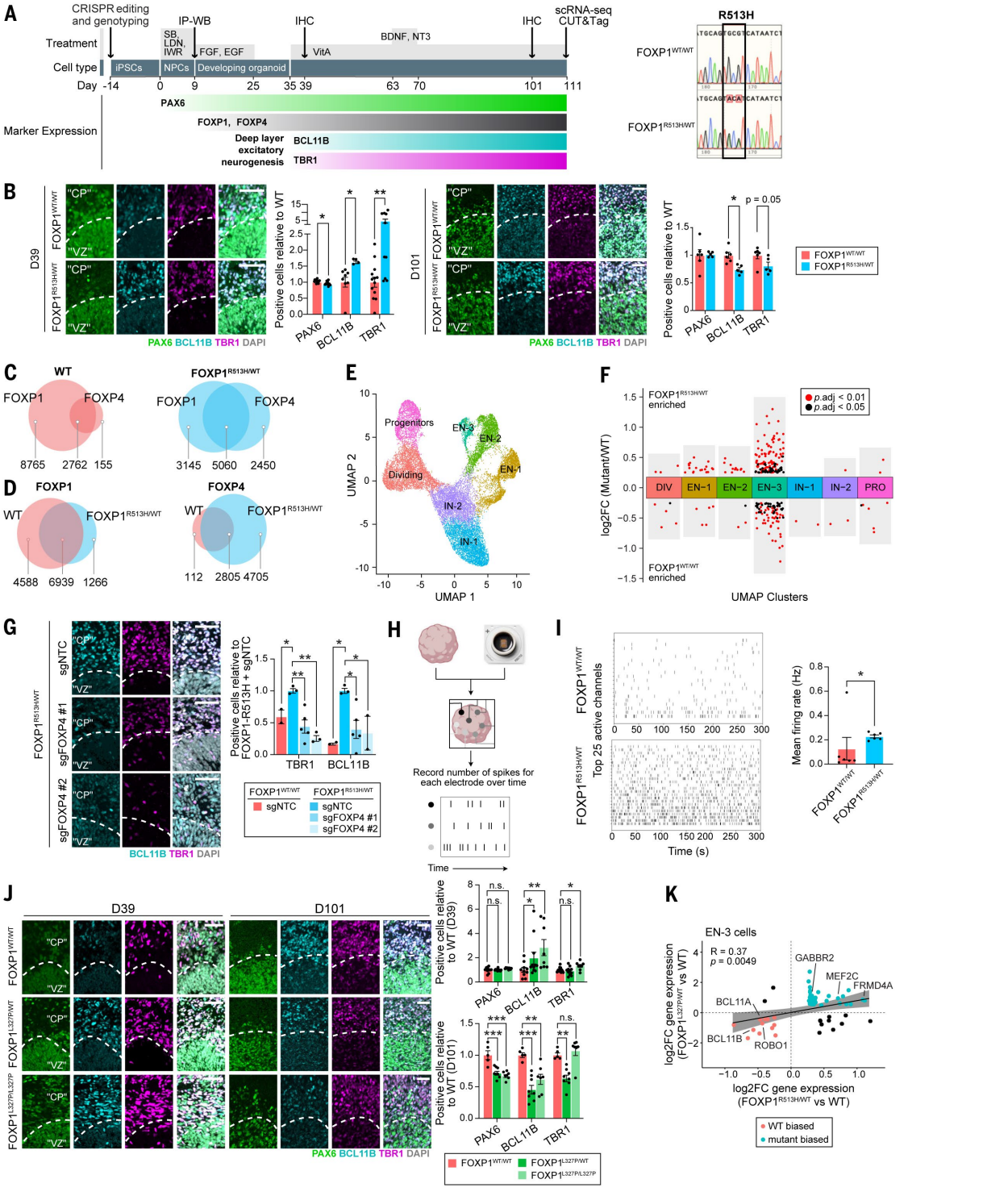

Fig. 8. hcASD variants alter deep-layer cortical neurogenesis in forebrain organoids. (**A**) Isogenic iPSC generation and differentiation workflows with validation (R513H; right). (**B**) Immunofluorescence images showing immunohistochemistry and quantification of PAX6$^+$, TBR1$^+$, and BCL11B$^+$ cells at day 39 and day 101 in FOXP1 R513H/WT versus WT. EGF, epidermal growth factor; FGF, fibroblast growth factor; IHC, immunohistochemistry; SB, SB431542 (neurotrophin-3 and brain-derived neurotrophic factor); IWR, IWR-1-endo (small molecule); LDN, LDN-193189 (small molecule); WB, Western blot. (**C** and **D**) CUT&Tag analysis showing DNA binding overlap (C) and genomic distribution (D) of FOXP1 and FOXP4. (**E** and **F**) scRNA-seq uniform manifold approximation and projection (UMAP) visualization (E) and cell type–specific DEGs (F) in day 111 organoids. (**G**) Immunofluorescence images showing rescue of the day 39 differentiation phenotype in FOXP1 R513H/WT upon FOXP4 KO. (**H** and **I**) Multielectrode array recordings (H) and representative raster plots (I). (**J**) Immunofluorescence images showing immunohistochemistry and quantification of the FOXP1 L327 allelic series (WT, heterozygous, homozygous) at day 39 and day 101. (**K**) Pearson's correlation of EN-3 DEGs between variants. In (B), (G), and (J), data were analyzed by linear mixed model (day 39) or linear regression (day 101) followed by permutation testing and Benjamini-Hochberg correction; $n = 10$ to 13 organoids [(B); day 39, day 101], $n = 2$ to 6 [(G); day 39, day 101], $n = 8$ to 11 [(J); day 39], and $n = 5$ to 8 [(J); day 101]. Data were analyzed by Wilcoxon rank-sum test with Bonferroni correction in (F) and by one-sided Mann-Whitney U test in (I) with $n = 6$ organoids. For bar graphs, data are means ± SEM. Scale bars are 50 μm. CP, cortical plate; VZ, ventricular zone–like. n.s. is not significant; *0.01 < P < 0.05; **0.001 < P < 0.01; and ***P < 0.001.

but this difference did not reach statistical significance after correcting for multiple comparisons. Concurrently, D101 FOXP1$^{R513H/WT}$ organoids exhibited an increase in SATB2^{+} neurons (fig. S10B). These results suggest premature differentiation of cortical neurons in FOXP1^{R513H} forebrain organoids, consistent with prior findings across multiple in vivo, in vitro, and in silico models (*22*, *59*, *77*, *78*).

To assess whether the mutation alters DNA binding, we performed CUT&Tag for FOXP1 and FOXP4 (*79*) (fig. S9B and table S8). In FOXP1$^{WT/WT}$ organoids, 94.7% of FOXP4 peaks overlapped with FOXP1 peaks (Fig. 8C), consistent with their function as a heterodimer. By contrast, only 67.4% of FOXP4 peaks overlapped with FOXP1-bound peaks in FOXP1$^{R513H/WT}$ organoids (Fig. 8C). Although 85% of FOXP1 peaks in FOXP1$_{R513H/WT}$ organoids overlap with those observed in FOXP1$^{WT/WT}$, only 37% of FOXP1$^{R513H/WT}$ FOXP4 peaks overlapped with those in FOXP1$^{WT/WT}$, with 4700 FOXP4 peaks in FOXP1$^{R513H/WT}$ organoids not found in controls (Fig. 8D). These findings suggest that FOXP1 missense variants affect FOXP4 function, with the loss of FOXP1-FOXP4 physical interaction leads to gain of FOXP4 binding at new genomic sites.

Using scRNA-seq, we identified DEGs between the mutant and WT organoids in ENs. We identified three EN clusters along the maturation trajectory: cortical deep layer 6 and subplate neurons (EN-3: high expression of *SOX5*, *NR4A2*, *TBR1*), deep layer 5/6 neurons (EN-2: high expression of *FOXP2*, *PBX3*, and *MEIS2*), and deep layer 5 neurons (EN-1: high expression of *FOXP1*, *ROBO1*, and *BCL11B*). The greatest number of DEGs were found in the EN-3 cluster (Fig. 8, E and F; and fig. S9, C and D), corresponding to the population displaying premature differentiation in FOXP1$^{R513H/WT}$ organoids (Fig. 8B). DEGs in EN-3 were enriched for FOXP1 and FOXP4 targets (fig. S9E), and up-regulated genes with reduced FOXP1 binding in CUT&Tag were enriched for hcASD+ (fig. S9F and table S8). Of EN-3 DEGs, 43% and 32% showed new FOXP1 and FOXP4 binding, respectively. Furthermore, 21% exhibited a "switch" from lost FOXP1 binding to new FOXP4 binding (fig. S9, F and G; and table S8). These findings suggested a gain of function or loss of specificity of FOXP4 in FOXP1$^{R513H/WT}$ organoids, potentially compensating for or compounding the loss of FOXP1 binding at these loci.

To determine whether the disrupted FOXP1-FOXP4 PPI could contribute to the cortical neurogenesis phenotype (fig. S9A), we generated double-mutant iPSC lines with a loss-of-function mutation in FOXP4 in the FOXP1$^{R513H/WT}$ background (FOXP1$^{R513H/WT}$-FOXP4^{KO}; fig. S9H). Forebrain organoids showed deep-layer neuron proportions similar to controls (Fig. 8F). These data suggest that a gain of FOXP4 function may account for the cortical neurogenesis defects in the FOXP1^{R513H} organoids. Thus, the R513H mutation represents not merely a simple loss of FOXP1 function, but a pathogenic gain of function for its disrupted interactor, FOXP4. Although the exact rescue mechanism needs to be determined, these data demonstrate that FOXP4 deletion suppresses the FOXP1 mutant phenotype.

To connect the cellular defects in FOXP1$^{R513H/WT}$ to functional properties, we recorded neural activity in organoids using multielectrode arrays. FOXP1$^{R513H/WT}$ organoids showed consistently higher mean firing rates than the isogenic control organoids (Fig. 8, H and I; and fig. S9I). Additional analyses of population-level parameters did not reveal changes in the spike time tiling coefficient, interspike intervals, and various burst metrics (fig. S9, J and K), suggesting alterations in baseline firing rather than network-wide properties. These results suggest that altered differentiation of cortical neurons observed in FOXP1$^{R513H/WT}$ organoids has functional consequences similar to those observed in independent studies of human stem cell–derived neuronal cultures harboring mutations in hcASD genes (*80*, *81*).

Finally, we examined whether iPSCs carrying the FOXP1^{L327P} mutation (fig. S10A), which resides at the predicted FOXP1-FOXP4 heterodimer interface and also leads to a loss of FOXP1-FOXP4 interaction, would phenocopy neurodevelopmental alterations identified in FOXP1$^{R513H/WT}$ organoids. Similar to FOXP1$^{R513H/WT}$, we found an increase in BCL11B during early neurogenesis and a decrease at the later time point (Fig. 8J) with a concurrent increase in SATB2^{+} neurons (fig. S10B) and a reduction of PAX6^{+} cells in both FOXP1$^{L327P/L327P}$ and FOXP1$^{L327P/WT}$ organoids (Fig. 8J). TBR1^{+} cells were likewise increased in FOXP1$^{L327P/L327P}$ early and decreased in FOXP1$^{L327P/WT}$ organoids at a later time point (Fig. 8J). DEGs identified using scRNA-seq in organoids during late neurogenesis showed concordant effect size and directionality between heterozygous FOXP1$^{L327P/WT}$ and FOXP1$^{R513H/WT}$ genotypes in the EN-3 cluster (Fig. 8K and fig. S10C). The abundance of γ-aminobutyric acid–containing (GABAergic) neurons was not altered in organoids with either the FOXP1^{L327P} or FOXP1^{R513H} mutation (fig. S10D), suggesting that the phenotypes were limited to the excitatory lineage. Thus, mutations that disrupt different structural domains of the FOXP1 protein phenocopy each other by destabilizing the FOXP1-FOXP4 heterodimer, leading to convergent phenotypes of premature progenitor exhaustion and aberrant deep-layer neurogenesis. Finally, to test whether cortical neurogenesis phenotypes are detected in the case of other ASD mutations, we introduced the E198K variant of high predicted pathogenicity (fig. S7E) into the endogenous locus of *PPP2R5D* (*82*). Consistent with findings for FOXP1 mutations, during early neurogenesis, PPP2R5D$^{E198K/E198K}$ organoids demonstrated a decrease in PAX6^{+} cells and an increase in BCL11B^{+} cells (fig. S10, E and F).

Discussion

Despite substantial progress in defining the genetic architecture of ASD, identifying causal molecular mechanisms and therapeutic targets has remained a central challenge (*10*, *83*). Efforts to identify convergent biology across hcASD genes have largely relied on transcriptomic analyses and low-throughput functional studies, leaving the proteomic landscape comparatively underexplored. In particular, whether and how genetically heterogeneous ASD risk genes organize at the level of protein complexes—and how disease-causing mutations perturb these interactions—remain poorly defined.

Here, we integrated large-scale human genetics, AP-MS, and AF-based structural prediction to map the physical interactome of proteins implicated in ASD. Mapping PPIs for 100 hcASD genes and 54 patient-derived missense variants in HEK293T cells enabled the depth, reproducibility, and scale required for comprehensive interactome mapping and systematic mutant interrogation, consistent with prior applications of this approach across diverse disease contexts (*12*–*19*). Multiple orthogonal lines of evidence support the disease relevance of these data, including strong overlap with neuronal interaction networks, high coexpression with hcASD genes in the developing human brain, selective enrichment for ASD—but not schizophrenia—risk genes, and functional validation moving from HEK293T cells to *Xenopus* and human brain organoids.

Our data reveal a dual-layered molecular architecture underlying ASD, where ASD risk proteins converge onto stable, shared protein complexes and independent ASD-associated mutations induce convergent patterns of interaction rewiring. Together, these layers provide a mechanistic bridge between genetic variation and neurodevelopmental dysfunction and nominate specific protein complexes, interactions, and interfaces as candidate therapeutic entry points. The ASD-PPI network highlights molecular modules not readily detectable by gene-centric genetic studies alone (*4*, *6*); identification of the PAF1 complex as a central hub illustrates how coherent protein assemblies can harbor multiple ASD-relevant components whose individual genetic signals fall below stringent significance thresholds.

Despite extensive genetic and phenotypic heterogeneity of ASD, the substantial interactor overlap among hcASD proteins suggests that a relatively limited set of molecular pathways may underlie core ASD biology, particularly for the severe end of the ASD spectrum that is markedly enriched for large-effect coding mutations (*4*, *8*, *84*, *85*). Although deleterious variants in the same genes have a very high degree of phenotypic variability, contributing to multiple neurodevelopmental conditions, including ASD, epilepsy, intellectual disability, and schizophrenia,

the ASD network described here exhibits distinctiveness for ASD, as evidenced by the absence of enrichment for schizophrenia risk genes. These findings raise the possibility that disease specificity may emerge not simply from gene identity but from how mutations perturb protein networks within developmentally relevant contexts.

Systematic comparison of WT and mutant PPIs revealed recurrent gain and loss of interactions across multiple hcASD variants, highlighting shared molecular vulnerabilities across genetically distinct mutations. Integration of AF predictions enabled identification of candidate interaction interfaces affected by disease-causing mutations. Although AF was not designed for interaction discovery, its performance in this context, particularly when leveraging consistency across predictions rather than maximum scores, outperformed conventional approaches and enriched for physiologically relevant interactions. Interactions observed across multiple cellular contexts were more likely to exhibit high AF confidence and mutation sensitivity, suggesting that broadly conserved interactions may represent core functional nodes.

Functional validation in human NPCs and forebrain organoids demonstrated that mutation-induced PPI rewiring has direct consequences on neurodevelopment. FOXP1 variants disrupted FOXP1-FOXP4 interactions, altered DNA binding, and promoted ectopic recruitment of FOXP4 to additional genomic loci. Despite high expression of FOXP1 in ganglionic eminences (*86*), we did not detect similar differences in GABAergic neurogenesis, potentially owing to compensation by other FOXP family members (*87*). Our data suggest that FOXP4, which is highly enriched in cortical but not subcortical progenitors (*27*, *77*), is responsible for altered glutamatergic neurogenesis. Altered cortical neurogenesis has been shown in recent reports using stem cell–derived models of ASD (*59*, *77*), and we also detected a similar trend in organoids with a missense mutation in *PPP2R5D*. Together, these findings underscore the importance of altered timing of cortical neurogenesis to ASD (fig. S10G), consistent with high coexpression of hcASD genes in these cell types (*4*, *22*), as well as findings from postmortem brain tissue (*88*).

Collectively, this study establishes a generalizable framework for mechanistic interpretation of genomic risk through PPI mapping. By integrating WT and mutant interactomes with structural modeling and human organoid systems, we enable causal inference at single-mutation resolution while maintaining the systemic context of the broader molecular landscape. Identification of both lost or weakened and aberrantly gained or strengthened interactions delineates complementary therapeutic strategies, including stabilization of disrupted complexes and inhibition of pathological interactions. More broadly, this platform prioritizes druggable protein interfaces and pathways, offering a rational foundation for precision therapies aimed at restoring neurodevelopmental trajectories and circuit-level function in ASD and establishing a generalizable blueprint for mechanistic drug discovery across neurological and psychiatric disease.

Materials and methods are available in the supplementary materials.

REFERENCES AND NOTES

1. C. Lord *et al.*, Autism spectrum disorder. *Nat. Rev. Dis. Primers* **6**, 5 (2020). doi: 10.1038/s41572-019-0138-4; pmid: 31949163
2. B. Tick, P. Bolton, F. Happé, M. Rutter, F. Rijsdijk, Heritability of autism spectrum disorders: A meta-analysis of twin studies. *J. Child Psychol. Psychiatry* **57**, 585–595 (2016). doi: 10.1111/jcpp.12499; pmid: 26709141
3. M. J. Maenner *et al.*, Prevalence and characteristics of autism spectrum disorder among children aged 8 years – Autism and Developmental Disabilities Monitoring Network, 11 sites, United States, 2020. *MMWR Surveill. Summ.* **72**, 1–14 (2023). doi: 10.15585/mmwr.ss7202a1; pmid: 36952288
4. F. K. Satterstrom *et al.*, Large-scale exome sequencing study implicates both developmental and functional changes in the neurobiology of autism. *Cell* **180**, 568–584.e23 (2020). doi: 10.1016/j.cell.2019.12.036; pmid: 31981491
5. B. Trost *et al.*, Genomic architecture of autism from comprehensive whole-genome sequence annotation. *Cell* **185**, 4409–4427.e18 (2022). doi: 10.1016/j.cell.2022.10.009; pmid: 36368308
6. J. M. Fu *et al.*, Rare coding variation provides insight into the genetic architecture and phenotypic context of autism. *Nat. Genet.* **54**, 1320–1331 (2022). doi: 10.1038/s41588-022-01104-0; pmid: 35982160
7. X. Zhou *et al.*, Integrating de novo and inherited variants in 42,607 autism cases identifies mutations in new moderate-risk genes. *Nat. Genet.* **54**, 1305–1319 (2022). doi: 10.1038/s41588-022-01148-2; pmid: 35982159
8. C. Lord *et al.*, The Lancet Commission on the future of care and clinical research in autism. *Lancet* **399**, 271–334 (2022). doi: 10.1016/S0140-6736(21)01541-5; pmid: 34883054
9. N. Sestan, M. W. State, Lost in translation: Traversing the complex path from genomics to therapeutics in autism spectrum disorder. *Neuron* **100**, 406–423 (2018). doi: 10.1016/j.neuron.2018.10.015; pmid: 30359605
10. H. R. Willsey, A. J. Willsey, B. Wang, M. W. State, Genomics, convergent neuroscience and progress in understanding autism spectrum disorder. *Nat. Rev. Neurosci.* **23**, 323–341 (2022). doi: 10.1038/s41583-022-00576-7; pmid: 35440779
11. J. F. Greenblatt, B. M. Alberts, N. J. Krogan, Discovery and significance of protein-protein interactions in health and disease. *Cell* **187**, 6501–6517 (2024). doi: 10.1016/j.cell.2024.10.038; pmid: 39547210
12. M. Kim *et al.*, A protein interaction landscape of breast cancer. *Science* **374**, eabf3066 (2021). doi: 10.1126/science.abf3066; pmid: 34591612
13. D. L. Swaney *et al.*, A protein network map of head and neck cancer reveals PIK3CA mutant drug sensitivity. *Science* **374**, eabf2911 (2021). doi: 10.1126/science.abf2911; pmid: 34591642
14. S. K. Hota *et al.*, Brahma safeguards canalization of cardiac mesoderm differentiation. *Nature* **602**, 129–134 (2022). doi: 10.1038/s41586-021-04336-y; pmid: 35082446
15. B. Gonzalez-Teran *et al.*, Transcription factor protein interactomes reveal genetic determinants in heart disease. *Cell* **185**, 794–814.e30 (2022). doi: 10.1016/j.cell.2022.01.021; pmid: 35182466
16. T. E. Tracy *et al.*, Tau interactome maps synaptic and mitochondrial processes associated with neurodegeneration. *Cell* **185**, 712–728.e14 (2022). doi: 10.1016/j.cell.2021.12.041; pmid: 35063084
17. J. Batra *et al.*, Protein interaction mapping identifies RBBP6 as a negative regulator of Ebola virus replication. *Cell* **175**, 1917–1930.e13 (2018). doi: 10.1016/j.cell.2018.08.044; pmid: 30550789
18. D. E. Gordon *et al.*, A SARS-CoV-2 protein interaction map reveals targets for drug repurposing. *Nature* **583**, 459–468 (2020). doi: 10.1038/s41586-020-2286-9; pmid: 32353859
19. S. Jäger *et al.*, Global landscape of HIV-human protein complexes. *Nature* **481**, 365–370 (2011). doi: 10.1038/nature10719; pmid: 22190034
20. H. J. Kang *et al.*, Spatio-temporal transcriptome of the human brain. *Nature* **478**, 483–489 (2011). doi: 10.1038/nature10523; pmid: 22031440
21. GTEx Consortium, Genetic effects on gene expression across human tissues. *Nature* **550**, 204–213 (2017). doi: 10.1038/nature24277; pmid: 29022597
22. A. J. Willsey *et al.*, Coexpression networks implicate human midfetal deep cortical projection neurons in the pathogenesis of autism. *Cell* **155**, 997–1007 (2013). doi: 10.1016/j.cell.2013.10.020; pmid: 24267886
23. G. Pintacuda *et al.*, Protein interaction studies in human induced neurons indicate convergent biology underlying autism spectrum disorders. *Cell Genom.* **3**, 100250 (2023). doi: 10.1016/j.xgen.2022.100250; pmid: 36950384
24. N. Murtaza *et al.*, Neuron-specific protein network mapping of autism risk genes identifies shared biological mechanisms and disease-relevant pathologies. *Cell Rep.* **41**, 111678 (2022). doi: 10.1016/j.celrep.2022.111678; pmid: 36417873
25. Y. Gao *et al.*, Proximity analysis of native proteomes reveals phenotypic modifiers in a mouse model of autism and related neurodevelopmental conditions. *Nat. Commun.* **15**, 6801 (2024). doi: 10.1038/s41467-024-51037-x; pmid: 39122707
26. T. Singh *et al.*, Rare coding variants in ten genes confer substantial risk for schizophrenia. *Nature* **604**, 509–516 (2022). doi: 10.1038/s41586-022-04556-w; pmid: 35396579
27. T. J. Nowakowski *et al.*, Spatiotemporal gene expression trajectories reveal developmental hierarchies of the human cortex. *Science* **358**, 1318–1323 (2017). doi: 10.1126/science.aap8809; pmid: 29217575
28. D. Szklarczyk *et al.*, The STRING database in 2021: Customizable protein-protein networks, and functional characterization of user-uploaded gene/measurement sets. *Nucleic Acids Res.* **49**, D605–D612 (2021). doi: 10.1093/nar/gkaa1074; pmid: 33237311
29. S. A. Aleksander *et al.*, The Gene Ontology knowledgebase in 2023. *Genetics* **224**, iyad031 (2023). doi: 10.1093/genetics/iyad031; pmid: 36866529
30. D. S. Manoli, M. W. State, Autism spectrum disorder genetics and the search for pathological mechanisms. *Am. J. Psychiatry* **178**, 30–38 (2021). doi: 10.1176/appi.ajp.2020.20111608; pmid: 33384012
31. K. E. McCluskey *et al.*, Autism gene variants disrupt enteric neuron migration and cause gastrointestinal dysmotility. *Nat. Commun.* **16**, 2238 (2025). doi: 10.1176/appi.ajp.2020.20111608; pmid: 33384012
32. S. Kaushik *et al.*, A tyrosine kinase protein interaction map reveals targetable EGFR network oncogenesis in lung cancer. bioRxiv 2020.07.02.185173 [Preprint] (2020); https://doi.org/10.1101/2020.07.02.185173.

33. D. Halder *et al.*, Suppression of Sin3A activity promotes differentiation of pluripotent cells into functional neurons. *Sci. Rep.* **7**, 44818 (2017). doi: 10.1038/srep44818; pmid: 28303954
34. A. Roopra *et al.*, Transcriptional repression by neuron-restrictive silencer factor is mediated via the Sin3-histone deacetylase complex. *Mol. Cell. Biol.* **20**, 2147–2157 (2000). doi: 10.1128/MCB.20.6.2147-2157.2000; pmid: 10688661
35. M. Quevedo *et al.*, Mediator complex interaction partners organize the transcriptional network that defines neural stem cells. *Nat. Commun.* **10**, 2669 (2019). doi: 10.1038/s41467-019-10502-8; pmid: 31209209
36. N. Ding *et al.*, Mediator links epigenetic silencing of neuronal gene expression with x-linked mental retardation. *Mol. Cell* **31**, 347–359 (2008). doi: 10.1016/j.molcel.2008.05.023; pmid: 18691967
37. M. J. Jurynec *et al.*, The Paf1 complex and P-TEFb have reciprocal and antagonist roles in maintaining multipotent neural crest progenitors. *Development* **146**, dev180133 (2019). doi: 10.1242/dev.180133; pmid: 31784460
38. C. Zhang *et al.*, The X-linked intellectual disability protein PHF6 associates with the PAF1 complex and regulates neuronal migration in the mammalian brain. *Neuron* **78**, 986–993 (2013). doi: 10.1016/j.neuron.2013.04.021; pmid: 23791194
39. N. J. Krogan *et al.*, RNA polymerase II elongation factors of *Saccharomyces cerevisiae*: A targeted proteomics approach. *Mol. Cell. Biol.* **22**, 6979–6992 (2002). doi: 10.1128/MCB.22.20.6979-6992.2002; pmid: 12242279
40. E. C. Ung, N. A. Borja, *LEO1* haploinsufficiency is associated with developmental delays and autism spectrum disorder. *J. Hum. Genet.* **71**, 109–111 (2026). doi: 10.1038/s10038-025-01410-5; pmid: 40993282
41. R. Evans *et al.*, Protein complex prediction with AlphaFold-Multimer. bioRxiv 2021.10.04.463034 [Preprint] (2022); https://doi.org/10.1101/2021.10.04.463034.
42. P. Bryant, G. Pozzati, A. Elofsson, Improved prediction of protein-protein interactions using AlphaFold2. *Nat. Commun.* **13**, 1265 (2022). doi: 10.1038/s41467-022-28865-w; pmid: 35273146
43. S. G. Choi *et al.*, Maximizing binary interactome mapping with a minimal number of assays. *Nat. Commun.* **10**, 3907 (2019). doi: 10.1038/s41467-019-11809-2; pmid: 31467278
44. Y.-C. Chen, S. V. Rajagopala, T. Stellberger, P. Uetz, Exhaustive benchmarking of the yeast two-hybrid system. *Nat. Methods* **7**, 667–668 (2010). doi: 10.1038/nmeth0910-667; pmid: 20805792
45. V. J. Heintz, L. Wang, D. J. LaCount, NanoLuc luciferase as a quantitative yeast two-hybrid reporter. *FEMS Yeast Res.* **21**, foab069 (2021). doi: 10.1093/femsyr/foab069; pmid: 34940882
46. X. Peng, J. Wang, W. Peng, F.-X. Wu, Y. Pan, Protein-protein interactions: Detection, reliability assessment and applications. *Brief. Bioinform.* **18**, 798–819 (2017). pmid: 27444371
47. P. Braun *et al.*, An experimentally derived confidence score for binary protein-protein interactions. *Nat. Methods* **6**, 91–97 (2009). doi: 10.1038/nmeth.1281; pmid: 19060903
48. P. Magini *et al.*, Loss of SMPD4 causes a developmental disorder characterized by microcephaly and congenital arthrogryposis. *Am. J. Hum. Genet.* **105**, 689–705 (2019). doi: 10.1016/j.ajhg.2019.08.006; pmid: 31495489
49. D. Yu, C. Cattoglio, Y. Xue, Q. Zhou, A complex between DYRK1A and DCAF7 phosphorylates the C-terminal domain of RNA polymerase II to promote myogenesis. *Nucleic Acids Res.* **47**, 4462–4475 (2019). doi: 10.1093/nar/gkz162; pmid: 30864669
50. F. Glenewinkel *et al.*, The adaptor protein DCAF7 mediates the interaction of the adenovirus E1A oncoprotein with the protein kinases DYRK1A and HIPK2. *Sci. Rep.* **6**, 28241 (2016). doi: 10.1038/srep28241; pmid: 27307198
51. Y. Miyata, E. Nishida, Identification of FAM53C as a cytosolic-anchoring inhibitory binding protein of the kinase DYRK1A. *Life Sci. Alliance* **6**, e202302129 (2023). doi: 10.26508/lsa.202302129; pmid: 37802655
52. D. Polioudakis *et al.*, A single-cell transcriptomic atlas of human neocortical development during mid-gestation. *Neuron* **103**, 785–801.e8 (2019). doi: 10.1016/j.neuron.2019.06.011; pmid: 31303374
53. A. Bhaduri *et al.*, An atlas of cortical arealization identifies dynamic molecular signatures. *Nature* **598**, 200–204 (2021). doi: 10.1038/s41586-021-03910-8; pmid: 34616070
54. R. Oughtred *et al.*, The BioGRID database: A comprehensive biomedical resource of curated protein, genetic, and chemical interactions. *Protein Sci.* **30**, 187–200 (2021). doi: 10.1002/pro.3978; pmid: 33070389
55. J. Xiang *et al.*, DYRK1A regulates Hap1-Dcaf7/WDR68 binding with implication for delayed growth in Down syndrome. *Proc. Natl. Acad. Sci. U.S.A.* **114**, E1224–E1233 (2017). doi: 10.1073/pnas.1614893114; pmid: 28137862
56. Q. Wang *et al.*, WDR68 is essential for the transcriptional activation of the PRC1-AUTS2 complex and neuronal differentiation of mouse embryonic stem cells. *Stem Cell Res.* **33**, 206–214 (2018). doi: 10.1016/j.scr.2018.10.023; pmid: 30448639
57. M. Lasser *et al.*, Pleiotropy of autism-associated chromatin regulators. *Development* **150**, dev201515 (2023). doi: 10.1242/dev.201515; pmid: 37366052
58. H. R. Willsey *et al.*, The neurodevelopmental disorder risk gene *DYRK1A* is required for ciliogenesis and control of brain size in *Xenopus* embryos. *Development* **147**, dev189290 (2020). doi: 10.1242/dev.189290; pmid: 32467234
59. A. Jourdon *et al.*, Modeling idiopathic autism in forebrain organoids reveals an imbalance of excitatory cortical neuron subtypes during early neurogenesis. *Nat. Neurosci.* **26**, 1505–1515 (2023). doi: 10.1038/s41593-023-01399-0; pmid: 37563294
60. S. Frendo-Cumbo *et al.*, DCAF7 regulates cell proliferation through IRS1-FOXO1 signaling. *iScience* **25**, 105188 (2022). doi: 10.1016/j.isci.2022.105188; pmid: 36248734
61. S. Najas *et al.*, DYRK1A-mediated cyclin D1 degradation in neural stem cells contributes to the neurogenic cortical defects in Down syndrome. *EBioMedicine* **2**, 120–134 (2015). doi: 10.1016/j.ebiom.2015.01.010; pmid: 26137553
62. A. Recasens *et al.*, Global phosphoproteomics reveals DYRK1A regulates CDK1 activity in glioblastoma cells. *Cell Death Discov.* **7**, 81 (2021). doi: 10.1038/s41420-021-00456-6; pmid: 33863878
63. V. Graham, J. Khudyakov, P. Ellis, L. Pevny, SOX2 functions to maintain neural progenitor identity. *Neuron* **39**, 749–765 (2003). doi: 10.1016/S0896-6273(03)00497-5; pmid: 12948443
64. N. C. Hettige *et al.*, FOXG1 dose tunes cell proliferation dynamics in human forebrain progenitor cells. *Stem Cell Reports* **17**, 475–488 (2022). doi: 10.1016/j.stemcr.2022.01.010; pmid: 35148845
65. S. F. Bellmaine *et al.*, Inhibition of DYRK1A disrupts neural lineage specificationin human pluripotent stem cells. *eLife* **6**, e24502 (2017). doi: 10.7554/eLife.24502; pmid: 28884684
66. K. E. Samocha *et al.*, Regional missense constraint improves variant deleteriousness prediction. bioRxiv 148353 [Preprint] (2017); https://doi.org/10.1101/148353.
67. E. L. Huttlin *et al.*, The BioPlex Network: A systematic exploration of the human interactome. *Cell* **162**, 425–440 (2015). doi: 10.1016/j.cell.2015.06.043; pmid: 26186194
68. M. Y. Hein *et al.*, A human interactome in three quantitative dimensions organized by stoichiometries and abundances. *Cell* **163**, 712–723 (2015). doi: 10.1016/j.cell.2015.09.053; pmid: 26496610
69. A. Calderone, L. Castagnoli, G. Cesareni, mentha: A resource for browsing integrated protein-interaction networks. *Nat. Methods* **10**, 690–691 (2013). doi: 10.1038/nmeth.2561; pmid: 23900247
70. K. Luck *et al.*, A reference map of the human binary protein interactome. *Nature* **580**, 402–408 (2020). doi: 10.1038/s41586-020-2188-x; pmid: 32296183
71. G. G. Tall, A. M. Krumins, A. G. Gilman, Mammalian Ric-8A (synembryn) is a heterotrimeric Gα protein guanine nucleotide exchange factor. *J. Biol. Chem.* **278**, 8356–8362 (2003). doi: 10.1074/jbc.M211862200; pmid: 12509430
72. C. A. Pearson *et al.*, Foxp1 regulates neural stem cell self-renewal and bias toward deep layer cortical fates. *Cell Rep.* **30**, 1964–1981.e3 (2020). doi: 10.1016/j.celrep.2020.01.034; pmid: 32049024
73. C. Bacon *et al.*, Brain-specific *Foxp1* deletion impairs neuronal development and causes autistic-like behaviour. *Mol. Psychiatry* **20**, 632–639 (2015). doi: 10.1038/mp.2014.116; pmid: 25266127
74. X. Li *et al.*, *Foxp1* regulates cortical radial migration and neuronal morphogenesis in developing cerebral cortex. *PLOS ONE* **10**, e0127671 (2015). doi: 10.1371/journal.pone.0127671; pmid: 26010426
75. A. Ortiz *et al.*, Cell type-specific roles of FOXP1 in the excitatory neuronal lineage during early neocortical murine development. *Cell Rep.* **44**, 115384 (2025). doi: 10.1073/pnas.1315710110; pmid: 24277810
76. T. Kadoshima *et al.*, Self-organization of axial polarity, inside-out layer pattern, and species-specific progenitor dynamics in human ES cell-derived neocortex. *Proc. Natl. Acad. Sci. U.S.A.* **110**, 20284–20289 (2013). doi: 10.1073/pnas.1315710110; pmid: 24277810
77. B. Paulsen *et al.*, Autism genes converge on asynchronous development of shared neuron classes. *Nature* **602**, 268–273 (2022). doi: 10.1038/s41586-021-04358-6; pmid: 35110736
78. H. R. Willsey *et al.*, Parallel in vivo analysis of large-effect autism genes implicates cortical neurogenesis and estrogen in risk and resilience. *Neuron* **109**, 788–804.e8 (2021). doi: 10.1016/j.neuron.2021.01.002; pmid: 33497602
79. H. S. Kaya-Okur *et al.*, CUT&Tag for efficient epigenomic profiling of small samples and single cells. *Nat. Commun.* **10**, 1930 (2019). doi: 10.1038/s41467-019-09982-5; pmid: 31036827
80. D. Trudler *et al.*, Dysregulation of miRNA expression and excitation in MEF2C autism patient hiPSC-neurons and cerebral organoids. *Mol. Psychiatry* **30**, 1479–1496 (2025). doi: 10.1038/s41380-024-02761-9; pmid: 39349966
81. F. P. McCready *et al.*, Hypersynchronous iPSC-derived SHANK2 neuronal networks are rescued by mGluR5 agonism. *Stem Cell Reports* **20**, 102718 (2025). doi: 10.1016/j.stemcr.2025.102718; pmid: 41270748
82. C. Loveday *et al.*, Mutations in the PP2A regulatory subunit B family genes *PPP2R5B*, *PPP2R5C* and *PPP2R5D* cause human overgrowth. *Hum. Mol. Genet.* **24**, 4775–4779 (2015). doi: 10.1093/hmg/ddv182; pmid: 25972378
83. A. J. Willsey *et al.*, The Psychiatric Cell Map Initiative: A convergent systems biological approach to illuminating key molecular pathways in neuropsychiatric disorders. *Cell* **174**, 505–520 (2018). doi: 10.1016/j.cell.2018.06.016; pmid: 30053424
84. I. Iossifov *et al.*, The contribution of de novo coding mutations to autism spectrum disorder. *Nature* **515**, 216–221 (2014). doi: 10.1038/nature13908; pmid: 25363768
85. S. J. Sanders *et al.*, Insights into autism spectrum disorder genomic architecture and biology from 71 risk loci. *Neuron* **87**, 1215–1233 (2015). doi: 10.1016/j.neuron.2015.09.016; pmid: 26402605

86. S. V. Precious *et al.*, FoxP1 marks medium spiny neurons from precursors to maturity and is required for their differentiation. *Exp. Neurol.* **282**, 9–18 (2016). doi: 10.1016/j.expneurol.2016.05.002; pmid: 27154297
87. N. I. Ahmed *et al.*, Compensation between FOXP transcription factors maintains proper striatal function. *Cell Rep.* **43**, 114257 (2024). doi: 10.1016/j.celrep.2024.114257; pmid: 38761373
88. T. Avino, J. J. Hutsler, Supernumerary neurons within the cerebral cortical subplate in autism spectrum disorders. *Brain Res.* **1760**, 147350 (2021). doi: 10.1016/j.brainres.2021.147350; pmid: 33607045
89. T. Li *et al.*, A scored human protein-protein interaction network to catalyze genomic interpretation. *Nat. Methods* **14**, 61–64 (2017). doi: 10.1038/nmeth.4083; pmid: 27892958
90. M. Giurgiu *et al.*, CORUM: The comprehensive resource of mammalian protein complexes-2019. *Nucleic Acids Res.* **47**, D559–D563 (2019). doi: 10.1093/nar/gky973; pmid: 30357367

ACKNOWLEDGMENTS

The authors thank T. Tolpa and A. Olmsted for graphic design support for figures and all members of the Psychiatric Cell Map Initiative (PCMI; U01MH115747) for their invaluable discussions and support. T.J.N. is a New York Stem Cell Foundation Robertson Neuroscience Investigator, and H.R.W. is a Biohub–San Francisco Investigator. The authors used ChatGPT-3 and Gemini to shorten text sections during the preparation of this manuscript. After using this tool and service, the authors reviewed and edited the content as needed and take full responsibility for the content of the publication. **Funding:** This work was funded by National Institutes of Health (NIH) grants U01MH115747 (to N.J.K., A.J.W., M.W.S., T.I., and T.J.N.), U01MH116487 (to A.J.W. and M.W.S.), 1OT2OD032742 (to N.J.K. and T.I.), U54CA274502 (to N.J.K. and T.I.), R01MH128364 (to T.J.N.), R01NS123263 (to T.J.N.), SF810018 (to T.J.N.), R25MH060482 (to N.J.K., A.J.W., M.W.S., T.I., and T.J.N.), and DP2OD040906 (to H.R.W.); Weill Institute for Neurosciences Startup Funding (to A.J.W.); a Weill Institute for Neurosciences Trailblazer Award (to A.J.W.); a Weill Institute for Neurosciences Weill Clinician-Scientist Award (to B.W.); a QBI Bold and Basic Award (to A.J.W.); California Institute for Regenerative Medicine (CIRM) DISC4-16322 (to T.J.N. and N.J.K.); the Overlook International Foundation (to M.W.S. and A.J.W.); Schmidt Futures (to T.J.N.); the William K. Bowes, Jr. Foundation (to T.J.N.); and a Sorensen Foundation Career Award in Child & Adolescent Psychiatry (to B.W.). **Author contributions:** N.J.K. is the lead contact. Conceptualization: M.W.S., N.J.K.; Methodology: B.W., R.V., Z.Z.C.N., K.M.H., B.J.P., A.B., M.B., U.C., J.A.K., L.S., D.L.S., T.J.N., R.H., A.J.W.; Software: B.W., Z.Z.C.N., K.M.H., B.J.P., A.B., M.B., Y.Zh., J.M., K.Z.G., P.W., M.C., M.G., D.F.B., S.A., P.P., D.P.; Validation: B.W., R.V., K.M.H., B.J.P., P.K., M.D.S., A.V.K.; Formal analysis: B.W., R.V., Z.Z.C.N., K.M.H., B.J.P., M.Bo., M.C.L., Y.Zh., J.M., U.C., J.A.K., M.C., M.G., S.A., S.L., M.Be., S.M., S.W., G.W., T.R.; Investigation: B.W., R.V., Y.Za., Z.Z.C.N., K.M.H., M.Bo., J.X., N.S., M.C.L., U.C., N.A., O.G., J.A.K., N.C., P.K., S.D., V.D., S.G., R.Th.,M.M., E.B., C.E., O.C., Y.L., R.M., M.S., T.Ba., R.K., J.A., T.R.; Data curation: B.W., Z.Z.C.N., B.J.P., A.B., M.Bo., K.Z.G., P.W., U.C., M.C., M.G., S.A., T.R.; Writing – original draft: B.W., R.V., Z.Z.C.N., K.M.H., B.J.P., A.B., M.E., K.O., T.J.N.; Writing – review & editing: B.W., R.V., M.E., R.To., S.C., K.O., T.J.N., M.W.S., A.J.W., N.J.K.; Visualization: B.W., R.V., Z.Z.C.N., K.M.H., B.J.P., A.B., M.E., M.Bo., M.C.L., U.C., J.A.K., S.A., D.P., S.Bal; Supervision: J.A.K., S.H.-J., J.S.F., T.Bo., S.F., C.D., S.Ban, N.M., T.I., P.B., H.R.W., R.H., K.O., T.J.N., M.W.S., A.J.W., N.J.K.; Project administration: K.O., T.J.N., M.W.S., A.J.W., N.J.K.; Funding acquisition: T.I., T.J.N., M.W.S., A.J.W., N.J.K. **Competing interests:** The Krogan Laboratory has received research support from Vir Biotechnology, F. Hoffmann–La Roche, and Rezo Therapeutics. N.J.K. has monetary and/or stock compensation with the following companies: GEn1E Lifesciences, Maze Therapeutics, Mreza Therapeutics, Rezo Therapeutics, and Tenaya Therapeutics. M.W.S. holds stock options in BeXorg and Echo Neurotechnologies; serves on the scientific advisory board and is a shareholder in MapLight Therapeutics; and serves on the board of directors and is a shareholder in Mreza Therapeutics. T.N., K.O., and R.To. are shareholders in Mreza Therapeutics. T.I. is a co-founder, is a member of the advisory board, and has equity interest in Data4Cure and Serinus Biosciences; and is a consultant for and has equity interest in Ideaya Biosciences and Eikon Therapeutics. **Data, code, and materials availability:** Further information and requests for resources and reagents should be directed to and will be fulfilled by corresponding author N.J.K. The raw AP-MS data files for both WT and mutant hcASD proteins have been deposited to the ProteomeXchange Consortium (http://proteomecentral.proteomexchange.org) via the PRIDE partner repository with the dataset identifier PXD047896. All raw scRNA-seq and CUT&Tag data from brain organoid experiments have been deposited in the Gene Expression Omnibus (GEO) (scRNA-seq: GSE285270, CUT&Tag: GSE285273). Code used for analysis has been deposited at GitHub (https://github.com/MattStateLab/asdppi). Any additional information required to reanalyze the data reported in this paper is available from the lead contact, N.J.K., upon reasonable request.

SUPPLEMENTARY MATERIALS

science.org/doi/10.1126/science.ady4523
Materials and Methods; Figs. S1 to S10; Tables S1 to S8; References (*91*–*132*); MDAR Reproducibility Checklist; Movie S1

Submitted 22 April 2025; resubmitted 26 February 2026; accepted 19 June 2026
10.1126/science.ady4523

Autism mutations rewire protein interaction networks to drive neurodevelopmental pathology

Belinda Wang, Rasika Vartak, Kelsey M. Hennick, Yefim Zaltsman, Zun Zar Chi Naing, Benjamin J. Polacco, Ali Bashir, Manon Eckhardt, Mehdi Bouhaddou, Jiewei Xu, Nawei Sun, Micaela C. Lasser, Yuan Zhou, Justin McKetney, Keelan Z. Guiley, Pawel Gniewek, Una Chan, Naufa Amirani, Owen Griffiths, Nishant Chadha, Reshmi Tognatta, Merve Cakir, Martin Gordon, Prachi Khare, Sam Drake, Vanessa Drury, David F. Burke, Silvano Gonzalez, Sahar Alkhairy, Reuben Thomas, Stephanie Lam, Montana Morris, Ethel Bader, Mélanie Dos Santos, Anastassia V. Komarova, Maxwell Bennett, Craig Ennis, Octavio Castillo, Yvonne Lim, Robert Martin, Meghan Seyler, Tierney Baum, Rebecca Krasnoff, George Wang, Sagnik Middya, Sheng Wang, Presley Pham, Juan Arbelaez, Dexter Pratt, Sofia Bali, Shivali Chag, Julia A. Kaye, Nadir Mahmood, Lee Spraggon, Thomas Rolland, Shawn Hervey-Jumper, James S. Fraser, Thomas Bourgeron, Steven Finkbeiner, Caroline Demeret, Danielle L. Swaney, Sourav Bandyopadhyay, Trey Ideker, Pedro Beltrao, Helen Rankin Willsey, Ruth Hüttenhain, Kirsten Obernier, Tomasz J. Nowakowski, Matthew W. State, A. Jeremy Willsey, and Nevan J. Krogan

Science **393** (6814), eady4523. DOI: 10.1126/science.ady4523

Editor's summary

A large number of genomic and transcriptomic datasets have revealed valuable insights into the biology of autism spectrum disorder (ASD). Wang *et al*. produced a complementary resource by mapping 100 high-confidence ASD genes and producing a large protein-protein-interaction (PPI) network, identifying more than 1800 interactions, most of which (87%) have never been reported previously. By integrating affinity purification–mass spectrometry data with AlphaFold-based structural predictions and by validating key interactions in human induced pluripotent stem cell–derived organoids and *Xenopus* embryos, the authors showed that disease-associated variants selectively weakened or strengthened specific PPIs, producing convergent neurodevelopmental phenotypes even when the variants reside in different genes. This study provides a valuable resource for understanding the biology of ASD. —Mattia Maroso